ABSTRACT

Title of thesis: PLANAR SLOW-WAVE STRUCTURE WITH PARASITIC MODE CONTROL

Long Bao Nguyen, Master of Science, 2014

Thesis directed by: Professor Thomas M. Antonsen, Jr.
Department of Physics
Department of Electrical and Computer Engineering

Modern vacuum tube devices dominate the field of high power and high frequency electronics. Among them, the Traveling Wave Tube Amplifier (TWTA) has broad bandwidth and consequently a wide range of applications. In this thesis, a planar sheath-like slow wave structure with rectangular geometry is studied and considered for use in a TWTA driven by a sheet electron beam. Although use of a wide sheet beam promises high power, the large transverse dimension of the structure risks interaction of the beam with multiple backward wave modes. Both the operating mode and the parasitic modes are analyzed using field theories with the planar sheath approximation. These solutions are then compared with finite element computations. Suppression of backward waves is then considered by designing the structure to preferentially absorb these waves. The results show good control of mode competition and high primary mode gain.

PLANAR SLOW-WAVE STRUCTURE WITH PARASITIC MODE CONTROL

by

Long Bao Nguyen

Thesis submitted to the Faculty of the Graduate School of the
University of Maryland, College Park in partial fulfillment
of the requirements for the degree of
Master of Science
2014

Advisory Committee:
Professor Thomas M. Antonsen, Jr., Chair/Advisor
Professor Thomas E. Murphy
Dr. Gregory S. Nusinovich

for my family

Acknowledgments

I am most thankful to Professor Thomas M. Antonsen Jr. for supervising the making of this thesis. The suggestions and directions Tom gave me are significant to the research's breakthroughs and the development of my scientific intuition. Inspirations also come from the fact that he generously allowed me to explore various scientific disciplines and was willing to discuss when his schedule allowed. His enthusiasm in tennis and theoretical physics is an integral ingredient of my life in graduate school.

I am glad ro receive the support from NRL and AFOSR, which is significant for the successful scientific results achieved in this thesis.

Dr. Gregory S. Nusinovich has been a dear leader in our group. Greg was always happy to spend his precious time motivating and helping me with required administrative procedures. His presence was an encouragement.

I want to give thanks to Professor Thomas E. Murphy and the scientists in IREAP for facilitating a vibrant and exciting scientific atmosphere. I owe my colleagues, especially Aydin C. Keser, Dmytro G. Kashyn and Elizabeth Tennyson, many hours of debates and discussions that helped broaden my knowledge and vision. I would have been a lost and wretched graduate student without the dedicated assistance from Ms. Melanie Prange, Ms. Dorothea Brosius, Mr. Ed Condon, and other staff members.

Finally, I would like to thank Quynh for keeping my graduate career in balance with her love and companionship.

Table of Contents

List of Tables

List of Figures

List of Abbreviations

Geometry

x_h	Dielectric region begins
x_v	Vanes begins
x_w	Conducting walls
p_z	Period in $\hat{z}$
p_y	Period in $\hat{y}$
L_z	Total length
L_z	Total width
α	Pitch of conducting sheets

Physical entities

$\vec{E}$	Electric field
$\vec{E}_t$	Transverse electric field
$\vec{E}_z$	Longitudinal electric field
$\vec{H}$	Magnetic field
$\vec{H}_t$	Transverse magnetic field
$\vec{H}_z$	Longitudinal magnetic field
$\vec{J}$	Current density
$\vec{J}_s$	Surface current density
$\vec{J}_b$	Beam current density
P	Power flux
ϵ	Electric permittivity
ϵ_o	Electric permittivity in free space
ϵ_r	Relative dielectric constant
μ	Magnetic permeability
μ_o	Magnetic permeability in free space
μ_r	Relative magnetic constant
c	Speed of light
v_b	Beam velocity
v_g	Wave's group velocity

Technical terms

RF	Radio-frequency
TWTA	Traveling Wave Tube Amplifier
SWS	Slow-Wave Structure
HFSS	High Frequency Structure Simulator

Non-technical terms

IREAP	Institute for Research in Electronics and Applied Physics
NRL	Naval Research Lab
AFOSR	Air Force Office of Scientific Research

Chapter 1

Introduction

1.1 The Traveling Wave Tube

When the term *"vacuum tube technology"* is mentioned, most of us reminisce about the old, bulky, familiar television set of the last century. Although such devices have disappeared from our everyday routines, demands for high-power (hundreds of watts) and high-frequency (higher than 10 GHz) amplifiers still require the design and production of vacuum tube devices. The range of power and operating frequencies of different amplifying technologies are shown on Fig. 1.1, indicating the ability of vacuum amplifiers to work in region of high power and high frequency. Several applications are reported on Fig. 1.2, ranging from commercial communication to fusion heating. Well-known modern types of tubes are the magnetron, the klystron, the gyrotron, the traveling wave tube (TWT), phototubes, and flourescent lamps [1], [2], [3].

Historically, the first generation of vacuum amplifiers were designed to operate

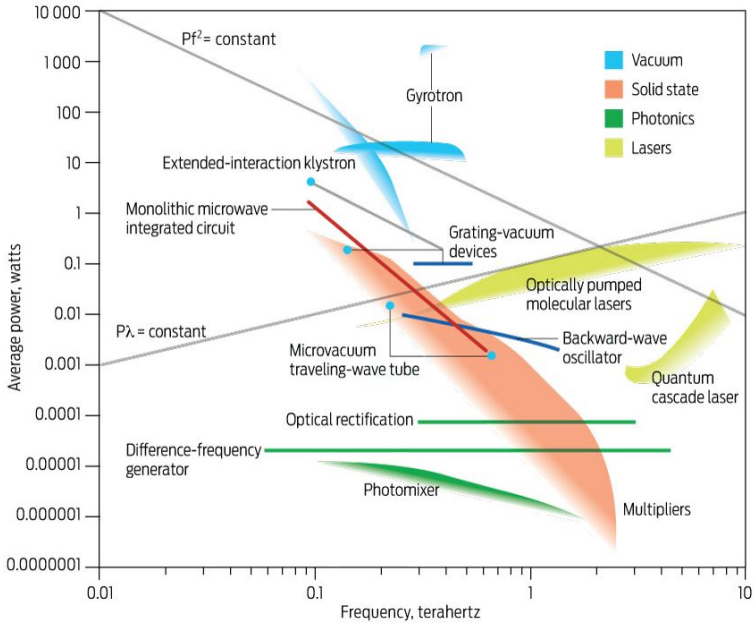

Figure 1.1: Range of power and frequency of different amplifying technologies [4]

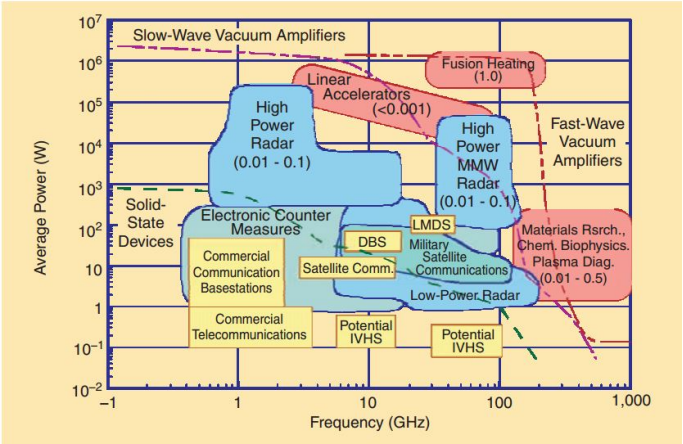

Figure 1.2: Application domain of various amplifiers, ranging from commercial telecommunications to fusion heating [2]

with three metal electrodes: two at the different ends of a tube to generate and collect the electron beams, one in the middle to provide control mechanism. The tube can be vacuum or gas-filled. These were known as vacuum tube triodes.

The working principle of a modern vacuum tube lies in the interaction between an electron beam and electric wave. Typically, two differently-charged electrodes are

used to generate the beam inside a vacuum tube or a tube filled with ionized gas at low pressure. Inside the tube, the beam of electrons is controlled by applying an electric field and/or magnetic field. [1]. At the same time, an electric wave is generated, which couples with the electron beam inside the tube, providing an amplifying mechanism. Fundamentally, the beam-wave interaction works as a conversion of spontaneous electromagnetic radiation to coherent radiation, which requires both synchronism condition and a condition for electron bunching [2].

Electron bunching mechanism is the core concept among the working principles of vacuum tubes and is the primary theory regarding slow-wave structure (SWS). It is illustrated in Fig. 1.3 [5]. As the velocity of the electron beam is slightly above the phase velocity of the RF wave, one group of electrons may slow down while another group may speed up. Together, if more electrons are decelerated than accelerated, they transfer their kinetic energy to the wave, thus amplify it. Bunching can be M-type or O-type. If bunching occurs by manipulating electrons' positions, it is classified as M-type. If it occurs by modulating electron momenta then it is O-type. M-type bunching is utilized in magnetron and cross-field amplifier while O-type devices include TWTAs and klystron [2].

Much research is being done to improve the performance of vacuum devices, each targeting specific component of the tube, such as designing better electrons emission and/or collection, attempting different fields manipulation techniques, and investigating beam-wave coupling [2]. Recent advances in computer simulation power and hardware fabrication techniques further drive the field of vacuum electronics forward, prompting new designs and novel concepts [3]. Among the different

types of vacuum tube amplifiers, the TWTA is a device of special interest due to its broad bandwidth, which results in its many applications in RF communication systems. A traditional TWTA is shown in Fig. 1.4. It primarily consists of the electron gun, RF input-output, the helix SWS, and the collector. Among the different components being researched on, the SWS is considered to have highest potential on the device's improvement.

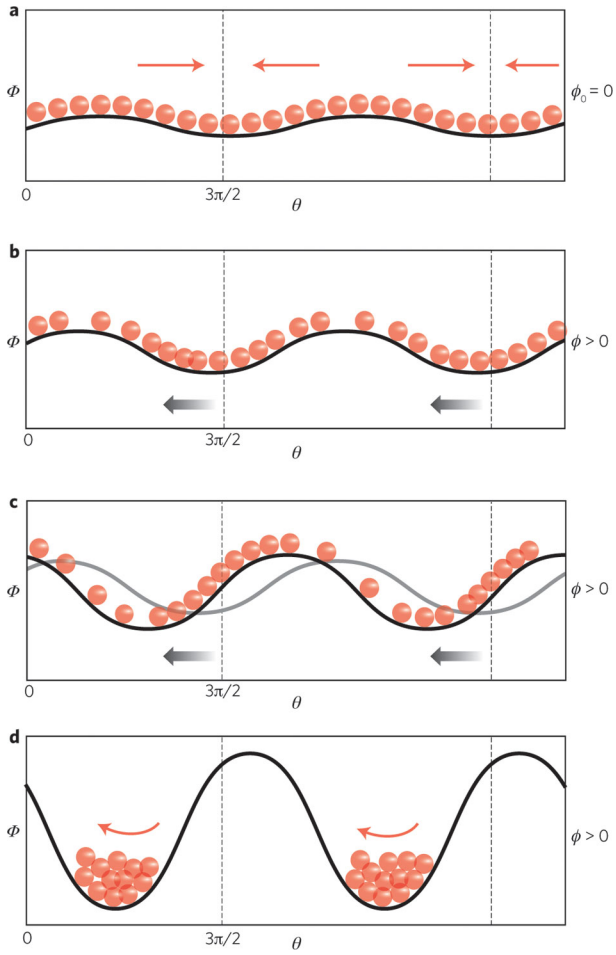

Figure 1.3: Electron bunching mechanism [5]

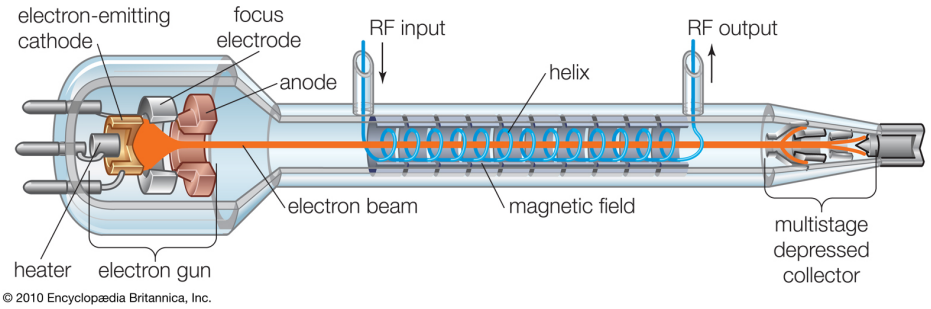

Figure 1.4: Classical Traveling Wave Tube Amplifier model with its main components [1]. Traditionally, the circularly wounded conducting wire, or helix, is used as the SWS

1.2 The Slow-Wave Structure

Slow-Wave structures are integral components in the operation of TWTA. The structure slows down the traveling wave's velocity to approximately that of the electron beam passing through the structure. This enables interaction between the beam and the wave to be amplified [6]. A fundamental feature of SWSs is that the beam must be placed near the structure, within a distance that is a fraction of the slow-wave length, to have a strong coupling. Thus, to increase beam power at fixed current density, extended or multiple beams must be considered. Recent advances in technology have made available sheet electron beams with large aspect ratios, which can provide higher beam power [3]. Furthermore, recent fabrication techniques provide methods to construct novel SWSs structure at small scales to accommodate high-frequency operation. A general difficulty in developing devices using sheet beams is that the large transverse size of the interaction region gives rise to unwanted modes that can interact with the beam [7], [8]. This is particularly true, as will be shown, for planar versions of helix structures. Thus, while planar versions of helix structures have been considered previously [9], [10], [11], [12], [13],

the fundamental problem posed by mode competition in large aspect ratio structures using sheet beams has not been addressed. The research work that embodies this thesis focuses on this issue. The goal is to design a structure that can provide wide bandwidth, accommodate a large aspect ratio sheet beam, and provide high gain while being immune to backward-wave instability.

A preliminary analysis and simulation of a sheath-like structure that can accommodate a sheet electron beam of the type generated at the Naval Research Laboratory (NRL) and used with a coupled cavity [7], [8], [14] was reported in [15] and [16]. Chapter 2 serves to summarize these results. Further investigation and designs with the goal to suppress parasitic modes were conducted and the findings were very successful. Chapter 3 describes the principles and implementation of mode control mechanism while chapter 4 and 5 envision the future development of this novel structure. The appendices give the reader a general idea of how the research is done analytically and computationally, in a way that future researchers can depend on these reports to further enhance the structure's operation with ease.

Chapter 2

Sheath Structure

2.1 Simple Model

A cut-away view of the central portion of the structure is shown in Fig. 2.1. It consists of two arrays of conducting wires backed by dielectric layers and conductors and separated by a vacuum region through which the electron beam will pass. The wire arrays have opposite pitches on the top and bottom layers. Here we take the z-axis to lie in the direction of the electron beam and the y-axis is in the long transverse direction. We first consider the properties of a doubly periodic portion of this structure. The example in Fig. 2.1 has ten periods in the y-direction and one period in z-direction. The lateral termination of the structure in the y-direction will be considered in chapter 3.

The field structure and dispersive properties of this configuration can be calculated approximately by replacing the periodic array of wires with an anisotropic conducting sheath that allows current to flow unimpeded in the direction of the wires and blocks the flow of current transverse to the direction of the wires. The fields in each of the three regions can be assigned common spatial wavenumbers in the $z-$ and $y-$ directions (k_z and k_y) and the dependences of the fields on x (the

short transverse direction) expressed in terms of hyperbolic trigonometric functions. Satisfying boundary conditions on the conducting surfaces and at the two sheaths then results in a transcendental dispersion relation giving frequency $\omega(k_z, k_y)$ as a function of the two wavenumbers and the parameters of the structure [15], [16]. A mathematical description of the dispersion relation can be found in Appendix A.

Fig. 2.2 shows a numerically generated dispersion plot for this model (frequency in GHz versus k_z in rad/cm) for two values of transverse wave number (k_y = 0 and 19.47 rad/cm) using the parameters listed in Table 2.1. The dimensions of the structure are chosen to be similar to the coupled cavity SWS recently built at NRL [7], [8], [14]. For the purpose of these calculations we choose a material with relative dielectric constant $\epsilon = 2.1$ and conductor pitch $\alpha = 0.362$ giving a phase velocity that matches the velocity of a 19.5 kV beam.

Parameter	$[mm]$
Period	
In z	0.23356
In y	0.6452
Tunnel height	0.7
Dielectric thickness	0.35
Conducting slab	
Width	0.12
Thickness	0.04

Table 2.1: Main Sheath Parameters

For the $k_y = 0$ case, which is characteristic of the operating mode, three solutions propagate down to zero frequency, one having even parity (in blue) and two having odd parity (in green). The even parity mode has a longitudinal electric field

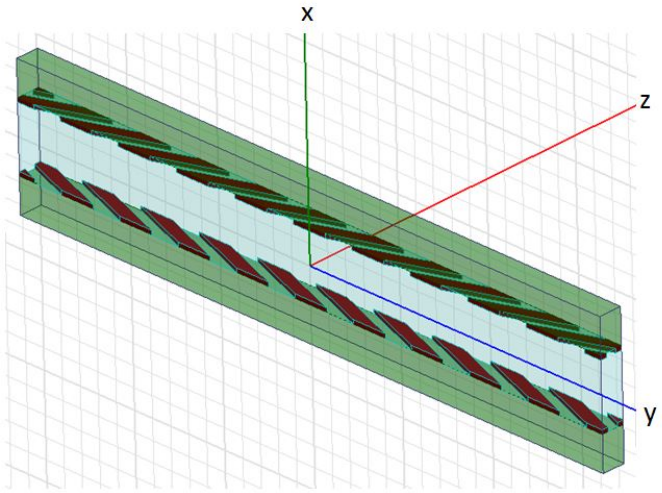

(a)

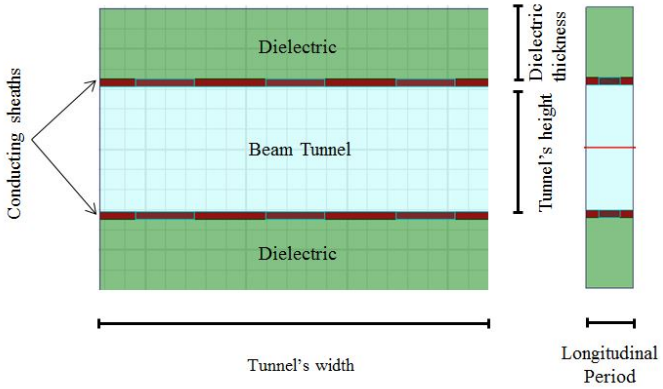

(b)

Figure 2.1: (a) Cut-away isometric view of a main sheath with one period in longitudinal direction and ten periods in transverse direction. (b) Cut-views design of the main structure

(E_z) that is symmetric with respect to x (the short transverse direction), whereas the longitudinal field for the odd parity modes is antisymmetric with respect to x. The even mode will interact strongly with the beam, and is considered to be the primary or operating mode.

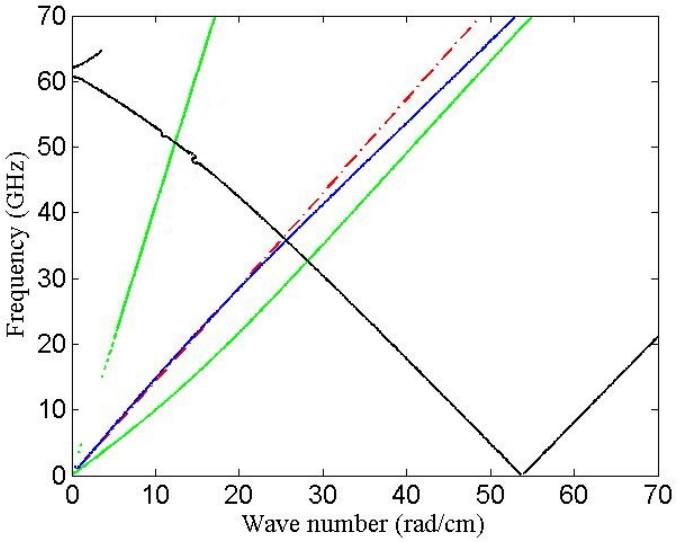

Figure 2.2: Dispersion plot based on analysis described in Appendix A

Also, shown in Fig. 2.2 is a dispersion curve for a mode with $k_y = 19.47$ rad/cm. It also propagates to zero frequency, but at a nonzero value of $k_z = 53.78$ rad/cm $\approx k_y/\alpha$. This solution represents modes with transverse variations that are potential competitors with the operating mode. We note that once variations in the $y-$direction are allowed ($k_y \neq 0$) then the modes no longer have even or odd symmetry. Furthermore, these solutions tend to be localized near either the top or bottom sheath. Therefore, for example, a low-frequency mode localized near the bottom sheath has the approximate dispersion relation $\omega = \nu_\phi|\alpha k_z - k_y|/(1+\alpha^2)^{1/2}$, where ν_ϕ is close to the speed of light. Localization near one of the sheaths has two consequences. First, since the mode is localized near a sheath, the fields available to interact with the beam are reduced. Second, the mode has a large group velocity ($v_{gy} = \partial\omega/\partial k_y$) in the long transverse direction. These two effects will be used to

reduce the danger of competition from these modes. The Pierce impedance [6]:

$$Z_p = \frac{\left|\int dz E_z(x,y) e^{-ik_z z}/p\right|^2}{2k_z^2 \int dxdy Re\left(\hat{z}\cdot\vec{E}\times\vec{H}^*\right)} \tag{2.1}$$

characterizes the strength of the beam-wave coupling. Here, p is the longitudinal period of the structure, and the integral of the Poynting flux is carried out over the cross section. For our simple model the period in the $z-$direction is arbitrary, and the impedance does not depend on this value. For definiteness, we take the structure to have a long transverse length of $L_y = 6.452$ mm to calculate the impedance. Values of impedance for the operating mode as a function of frequency are shown in Fig. 2.3(a). Also shown are values of impedance for a competing backward-wave mode at the same frequency. For this plot, k_y is varied to produce an intersection with the operating mode dispersion relation at each frequency.

If we assume representative values for the beam voltage ($V = 19.5$ kV) and current ($I = 3.5$ A), shown in Table 2.2, the Pierce gain parameter C can be calculated. The results for the operating and competing modes are plotted also in Fig. 2.3(b).

Measurement	*Value*
Voltage	19.5 kV
Current	3.5 A

Table 2.2: Beam parameters of interest

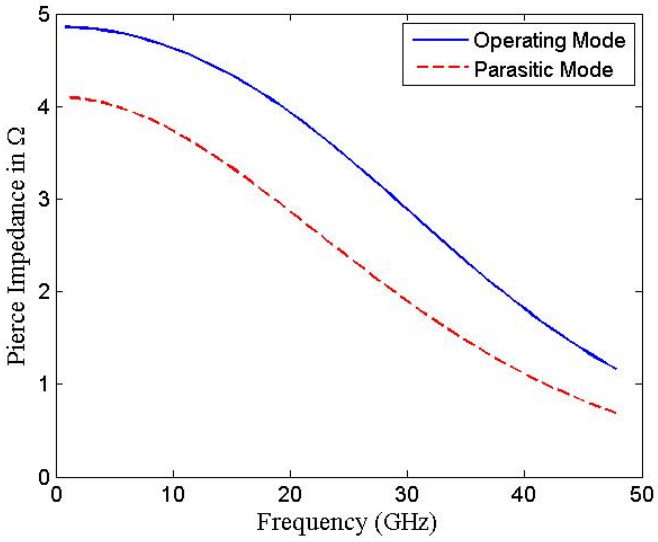

(a)

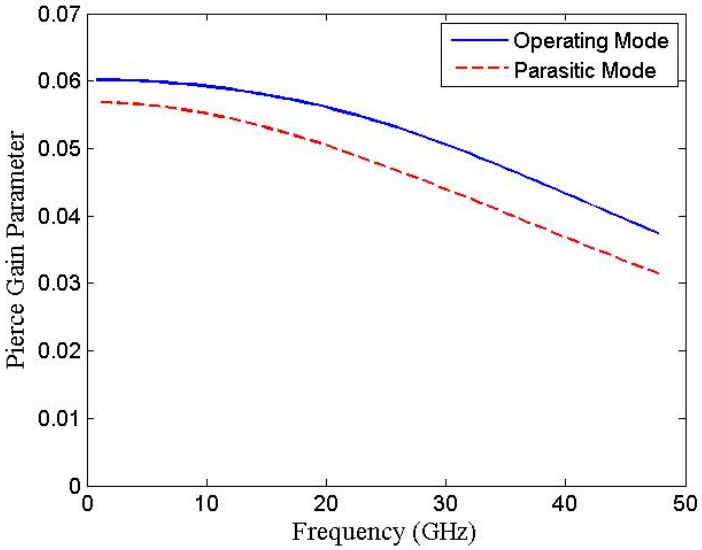

(b)

Figure 2.3: (a) Pierce impedance and (b) Pierce gain parameter of operating mode and a representative parasitic mode based on the analysis in Appendix A

2.2 Periodic Model

To test our simple model we have used the commercial software HFSS to calculate the eigenmodes of the doubly periodic structure shown in Fig. 2.1. Master-slave

boundary conditions in both longitudinal and transverse directions were applied. We specified periodic boundary conditions in the transverse direction and varied the phase advance in the longitudinal direction. The results are displayed as a sequence of points on Fig. 2.4. Also shown in Fig. 2.4 are solutions from the sheath model plotted for several values of $k_y = 2n\pi/L_y$, confirming our prediction that parasitic backward-waves arise due to the presence of modes with variations in the long transverse direction [15], [16]. As can be seen, the simple model agrees well with the HFSS solutions. We also note that in the HFSS calculation the conductors had a thickness of 0.04 mm, whereas in the analytical model, the thickness was taken to be zero, so the dimensions of the conducting slabs have no effect on the dispersion property of the structure. Thus, our understanding of the structure based on the simple model can be used to design a planar slow-wave device.

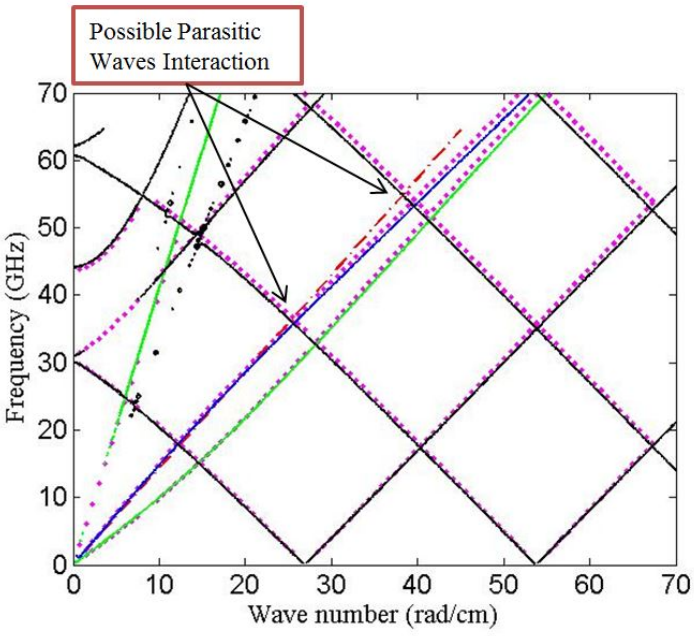

Figure 2.4: Dispersion plot for the structure in Fig. 2.1 from HFSS (dots) and from analysis based on equations in Appendix A (solid line)

Chapter 3

Mode Suppression

3.1 Principles

Our approach to suppression of the competing backward-waves is based on the observation that in the doubly periodic structure of Fig. 2.1, these waves have large group velocities in the long transverse direction, whereas the operating mode has zero group velocity in this direction. This difference will be exploited as follows. We construct a structure with a central region having one spacing (sheath height) between the two wire arrays where the beam will propagate. Connected to this region, on either side, are side tunnels with a smaller spacing (side tunnel height). At the edges of the side tunnels the conductors on the upper and lower sheaths are joined to close the current paths. The dielectric supporting the conductors in the side regions is made to be more lossy than that in the beam tunnel region. The whole structure is then enclosed in a conducting rectangular waveguide. This situation is shown in Fig. 3.1, where the dielectrics and conductors are shown but not the enclosing waveguides. The darkened dielectric indicates where the loss is high. The difference in sheath spacing will exclude the fields of the operating mode from the side tunnel regions. The beam and the operating mode will occupy the central

region. The competing backward-wave modes, which have large group velocities in the long transverse direction, and which tend to be localized near a sheath, will freely extend into the side regions. This will act to reduce the Pierce impedance for the competing modes relative to the operating mode, because the power in the denominator of Eq. (2.1) is extended over a larger area for the competing modes. In addition the higher value of loss in the dielectric in the side regions will serve to increase the attenuation of the competing modes relative to the operating modes. The dimensions and parameters of our composite structure are given in Table 3.1. The model is shown in Fig. 3.1.

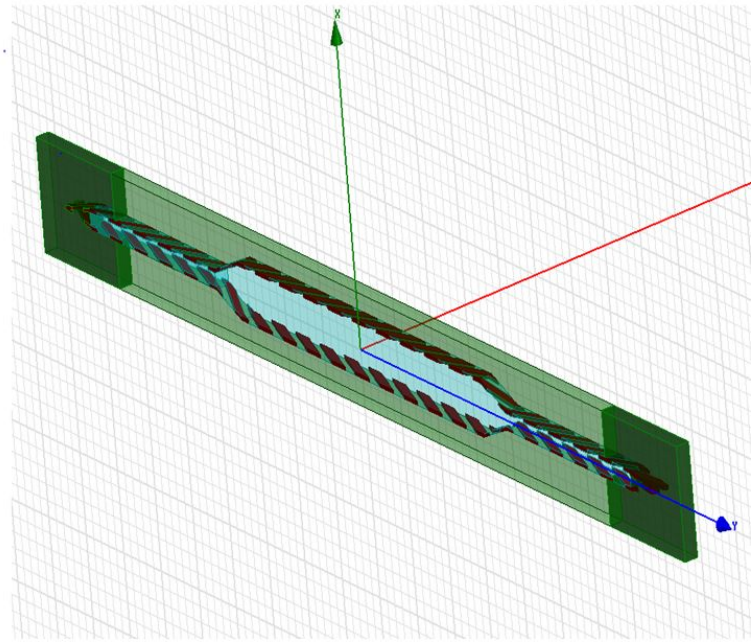

Figure 3.1: Composite connected sheath structure showing beam region, side region, and lossy dielectric in dark

Measurement	$[mm]$
Period	
In z	0.23356
In y	0.6659
Tunnel height	0.24
Dielectric thickness	0.58
Conducting slab	
Width	0.12
Thickness	0.04

Table 3.1: Side Parameters - Connected Sheath

3.2 Implementation

The dispersion relation for the modes of the structure in Fig. 3.1 is displayed in Fig. 3.2. The properties of the modes are similar to those of the doubly periodic structure. Specifically, there is an operating mode, which has a relatively linear dependence of frequency on wave number, and can be expected to yield amplification over a broad band of frequencies. In addition there are competing backward wave modes that can be associated with variations of the fields in the long transverse direction. We have labeled two modes in the vicinity of 35 GHz on Fig. 3.2. The mode labeled a) is an operating mode and the mode labeled b) is a backward wave competitor. The structure of the modes is illustrated in Fig. 3.3 where we have plotted the y-dependence of the Pierce impedance $Z_p(x = 0, y)$ defined in Eq. (1) . It can be seen that for the operating mode a) the fields reside mainly in the central region, are relatively uniform in y, and give rise to a coupling impedance that is about 3.63 Ohms in the sheath region. For the competing mode b) the fields ex-

tend into the side region and exhibit a standing wave pattern in the central region. The average parasitic coupling impedance in the central region is 1.23 Ohm. The extension of the parasitic mode fields into the side regions allows these modes to be preferentially damped. We have given the dark colored dielectric in Fig. 3.1 a loss tangent value of 0.75 and adjusted the voltage value to 30.6 kV and current to 4 A, shown in Table 3.2, to facilitate good coupling between the beam and the primary mode. These parameters result in attenuation values for the operating mode of 0.71 dB/cm and values for the backward wave mode of 5.97 dB/cm. These values, in conjunction with the computed coupling impedances, can be used to estimate the maximum stable length for our structure. We find, based on the analysis of [17], that the maximum stable length is 3.8 cm. From [18], [17], analyzing the amplitudes of three waves corresponding to the operating mode using the length above gives a primary gain of 20dB. The three-mode approach for gain calculation is explained in Appendix A. HFSS technique to collect and analyze data is summarized in Appendix B.

Parameter	*Value*
Voltage	30.6 kV
Current	4 A

Table 3.2: Beam parameters used for the connected sheath structure.

To investigate the bandwidth property of the structure, we have applied the dispersion data obtain in Fig. 3.2 of the primary mode to our Pierce analysis and

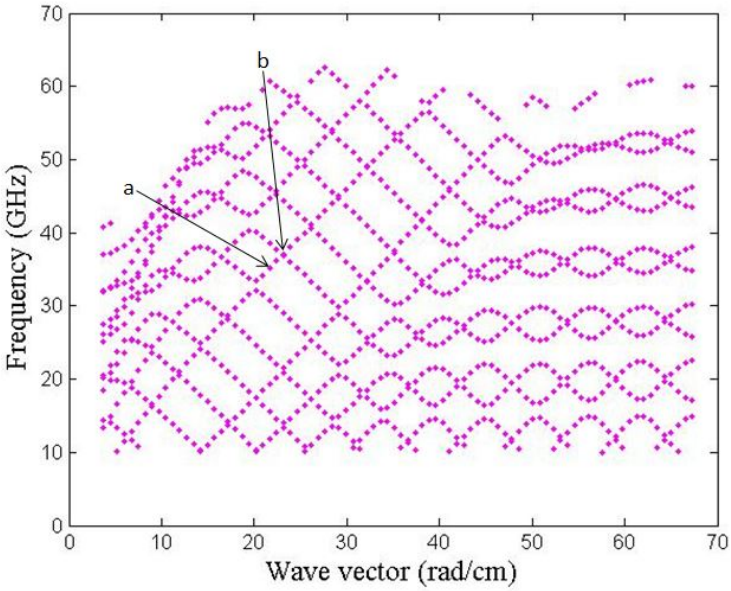

Figure 3.2: Dispersion plot from HFSS data for composite connected sheath structure of Fig. 3.1 with (a) representing primary interaction between beam and operating mode and (b) representing parasitic interaction between beam and backward-wave mode

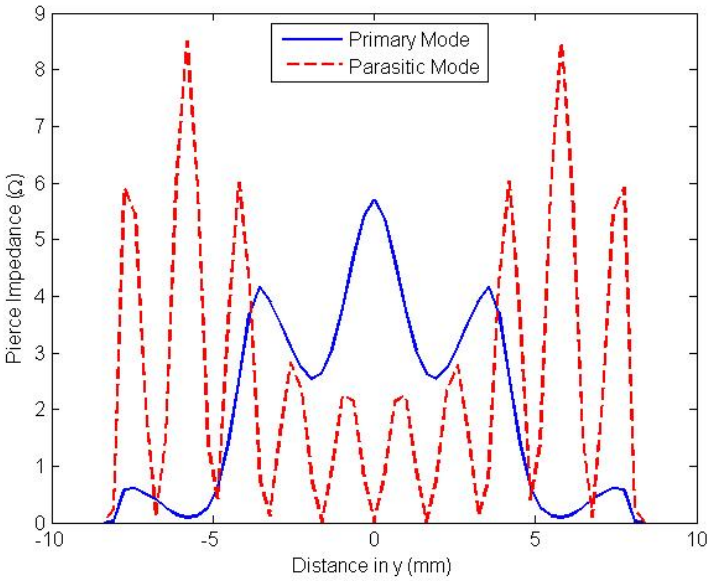

Figure 3.3: Pierce impedance profile of operating and parasitic modes (labeled(a) and (b) in Fig. 3.2) of connected sheath structure

also obtained the simulated coupling impedance from HFSS. The results are plotted in Fig. 3.4 with blue line representing the analytical and red crosses representing

the simulated impedance. This shows that the simulation results are in the range of our analysis. We then calculated and plotted the small signal gain of the structure over a wide range of frequencies in Fig. 3.5. The result shows a high and steady gain from 35GHz to 50GHz.

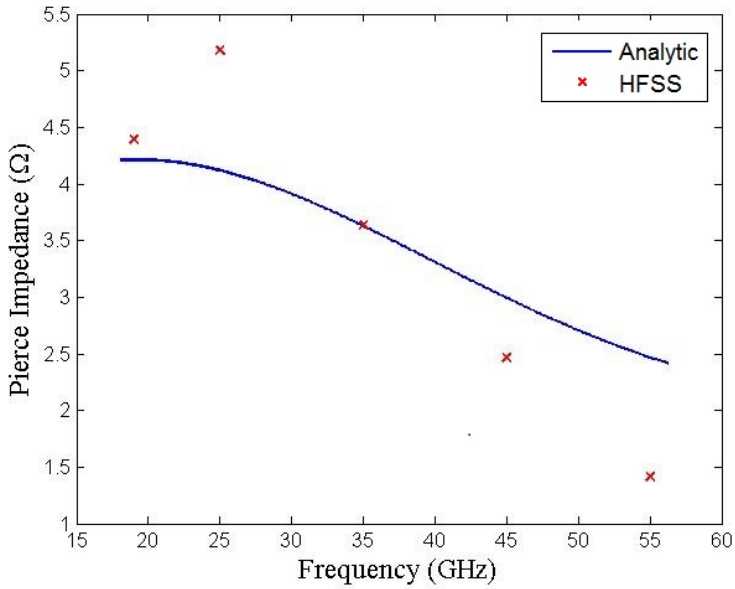

Figure 3.4: Pierce impedance of operating mode for connected sheath structure; analysis result is shown as solid line. HFSS results are shown as crosses

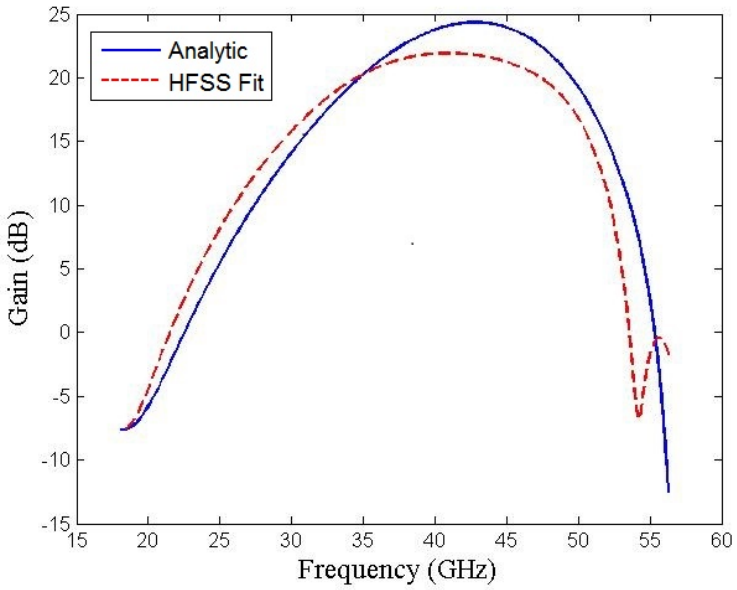

Figure 3.5: Small signal gain of the connected structure shown in Fig. 3.1, based on analytical model of Pierce impedance (solid line) and HFSS calculation of impedance (dashed line)

Chapter 4

Prologue to the Future

The structure proposed in chapter 3 gives rise to two intriguing issues that require further consideration. Firstly, since the pitch and dielectric thickness of the side regions are different from the initial design, the dispersion characteristic of the structure is now different (Fig. 3.2 vs Fig. 2.4). The primary wave doesn't have strong interaction with the beam of interest (with voltage source equal to 19.5 kV) anymore, resulting in the need to tune the source voltage to more than 30 kV. Secondly, we speculated that the parasitic starting length can be made longer by adding more lossy material on the side, particularly by widening the structure in transverse direction with lossy material. These considerations leaded to the new design as proposed below.

In this structure (Fig. 4.1), the pitches in both the central and side regions are tuned, in a ratio that is approximately 2/1, to values lower than those in chapter 3. Pitches equal to 0.31 for the central region and 0.315 for the side regions, resulting in the dimensions shown in Table 4.1. Additionally, the sides are made to be twice as large. The added volume is made of the same lossy meta material (in dark color) from chapter 3.

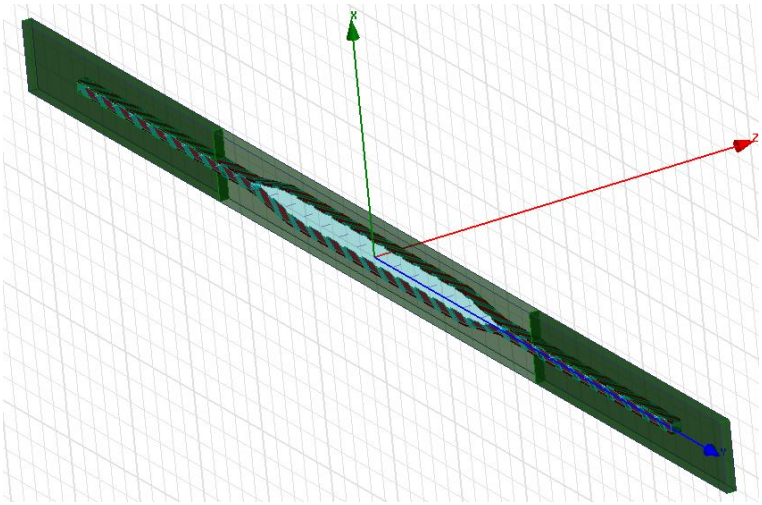

Figure 4.1: Proposed disconnected sheath structure with wider sides which consist of higher volume of lossy material

Parameter in mm	*Central region*	*Side regions*
Period		
In z	0.2	0.2
In y	0.6452	0.6349
Tunnel height	0.7	0.24
Dielectric thickness	0.35	0.58
Conducting slab		
Width	0.12	0.12
Thickness	0.04	0.04

Table 4.1: Disconnected sheath structure's parameters

Another novel feature of this structure is the open-ended sides: the conductors on the top and bottom do not make electrical contact. Since the wavelength of interest is larger than the height of the sheath, the open sides act as a conducting connection between the top and bottom sheets. This phenomenon allows the structure to be fabricated easily and efficiently. We call it the disconnected sheath structure.

The dispersion relation for this new structure is shown in Fig. 4.2. The

operating mode (blue line) has a similar slope to that of Fig. 2.4, implying that its phase velocity is approximately the same. This results in a strong interaction between the primary even wave and the electron beam which has relatively low source voltage ($\leq$ 19.5 kV). This dispersion characteristic is similar to that of a structure with side connection, confirming our conclusion regarding the open sheath feature. The Pierce impedance profile in the transverse direction is presented in Fig. 4.3. Blue solid line represents primary mode at 35 GHz. Red dashed line represents a parasitic mode at 36 GHz. The result shows a strong primary interaction in the central region, where the beam is present, while the parasitic waves are kept to the lossy regions on the sides. This is similar, but clearly an improvement, to the profile plotted in Fig. 3.3.

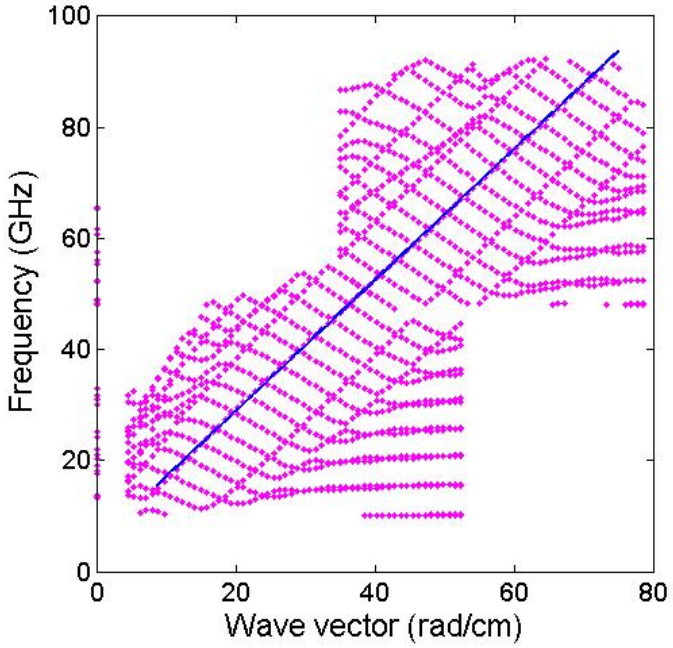

Figure 4.2: Dispersion relation for the disconnected sheath structure. HFSS simulation result is shown in purple dots. The blue line is a fitted-curve representing the primary mode

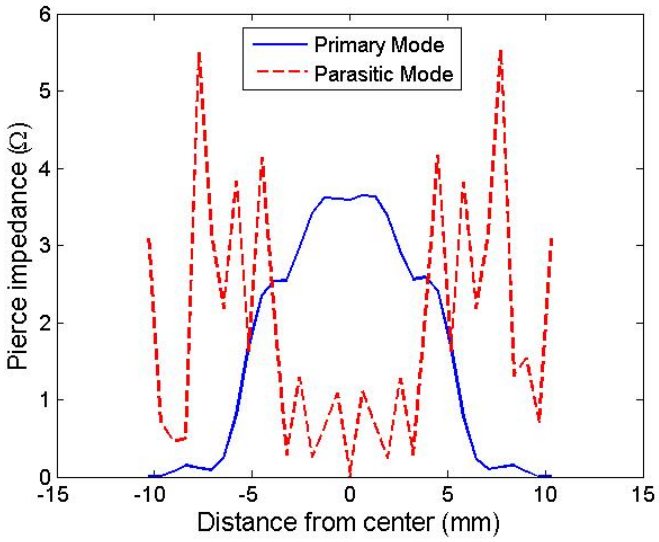

Figure 4.3: Pierce impedance across transverse direction for the disconnected sheath structure. Blue solid line represents primary mode at 35GHz. Red dashed line represents a parasitic mode at 36GHz

The added volume of lossy material results in significant parasitic waves' attenuation. The loss rate for them are shown in Fig. 4.4. While the loss rate for the primary mode stays at 5 dB/cm, the one for parasitic modes increases almost linearly with frequency. Using the analysis from [18] and [17], summarized in Appendix A, the starting length was computed to be infinity.

Assuming a source voltage of 18.5 kV and beam current of 4 A, the Pierce gain parameter for primary mode is computed and plotted in Fig. 4.5. The result from our simple model analysis is shown as the blue line while the HFSS data is curve-fitted and presented as the dash red line. This reflects the proximity between them, proving the success of the field theory approach in studying the structure.

The corresponding primary gain is calculated and plotted in Fig. 4.6 using a representative length $L_z = 4$ cm. The gain characteristic of the structure can

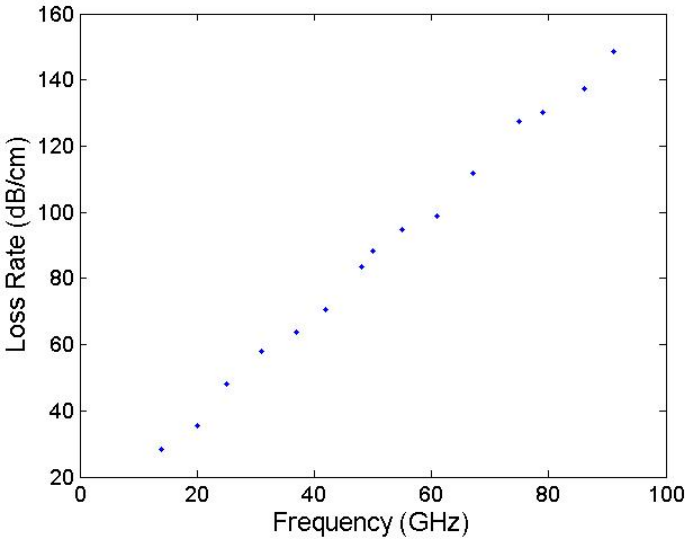

Figure 4.4: Loss rate of parasitic modes at different frequencies for the disconnected sheath structure

Measurement	*Value*
Voltage	18.5 kV
Current	4 A

Table 4.2: Beam parameters used for the disconnected sheath structure.

be modified at ease by varying the source voltage or changing the structure's total length. Different applications with various demands on gain and bandwidth can utilize the same SWS.

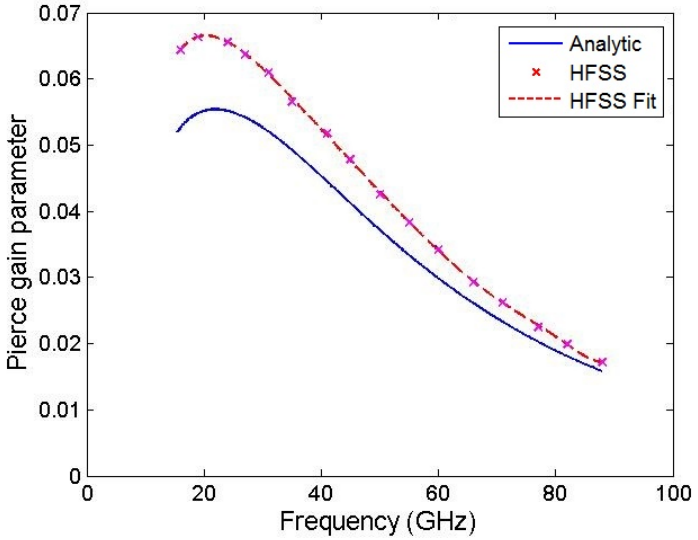

Figure 4.5: Pierce gain parameter for the disconnected sheath structure. Result from analysis is represented in blue solid line. HFSS data is marked as purple crosses, and the fitted curve is in red dashed line

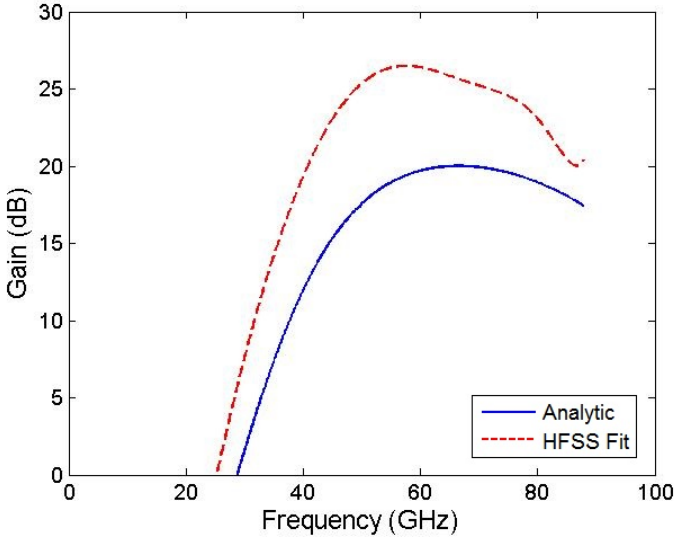

Figure 4.6: Bandwidth of the disconnected sheath structure

Chapter 5

Summary

This thesis introduces the novel planar slow-wave structure to be used with a sheet electrons beam, which promises high power output. The geometry of this structure allows it to be treated analytically using field theory (Appendix A, [18]), as opposed to circuit theory developed previously ([6], [17]). It is also easy to fabricate such a rectangular device at sub-millimeter scale using current technology. Chapter 2 demonstrated that the structure's parameters can be tuned to allow operation within the desired range of frequency. The theory also described the potentially unstable parasitic modes and suggested a means to suppress them. Chapter 3 investigated an approach to control parasitic waves. Chapter 4 followed up by proving that such a method can be used to increase the parasitic starting length to infinity, which guarantees stable operation. Moreover, the disconnected structure as proposed in chapter 4 shows a potential for high gain and broad bandwidth. It is a strong candidate to be used in future generations of radar and satellite communication systems.

An other type of slow-wave structure that is compatible with the sheet electrons beam is the coupled cavity, investigated previously in [8]. The cavity proposed

there has a parasitic starting length equal to 6.6 cm, while a 3.2 cm long structure of its kind has a gain of 10.2 dB. The planar sheath slow-wave structure is obviously an improvement.

With the theory well-developed and the principles of the structure studied, the task at hand is to investigate an input-output waves coupling scheme. Additionally, thermal heating from the high power input, together with techniques to limit it, will be explored.

Appendix A: Theoretical Derivations

This appendix presents the derivation of the analytic wave solutions and modes of the planar structure. The most important result is the dispersive behavior of the waves because it affects how strong the beam-wave coupling we can achieve and how waves propagate inside. It is then followed by formulation of the Pierce impedance and the gain calculation utilizing the three-wave theory.

Although a pedagogical approach should start with a simple case in which there is no wave propagation in the transverse direction (see [15], for instance), I prefer a full description treatment. The physical model is analyzed with wave propagation in both directions. The single cell case is then described as a special case by letting $k_y = 0$.

In the Pierce impedance derivation, we note that the dispersion relation can also be derived using admittance matrices. This approach is more convenient to work with if one has a computational software package that is based on linear algebra such as MATLAB, though less intuitive.

A.1 Dispersion Characteristics

A.1.1 Formalation

Define $\hat{z}$ to be the longitudinal direction and $\hat{y}$ to be the long transverse direction. The geometry of the structure then depends only on x. Define the pitch of the conducting sheaths on the planar surfaces of the sheath as α, where

$$\alpha = \frac{dz}{dy}$$

on top, $x = x_h$ and

$$\alpha = -\frac{dz}{dy}$$

on bottom, $x = -x_h$. At this point, we assume the sheath extends infinitely in the $\hat{y}$ and $\hat{z}$ directions. Geometrically, let p_z and p_y be the period of the sheaths in longitudinal and transverse directions respectively, then

$$\alpha = \frac{p_z}{p_y}$$

Define a Cartesian coordinate system with the origin at the center of the x-y surface of the structure, as depicted in Fig. A.1. The geometry of the structure with respect to $\hat{x}$ is defined as follows:

x_h	dielectric region begins
x_v	vanes region begins
x_w	conducting wall

Dielectric layers ($x_w > |x| > x_h$) serve to support the conducting sheaths that surround the vacuum region where the beam passes. We also allow the possibility

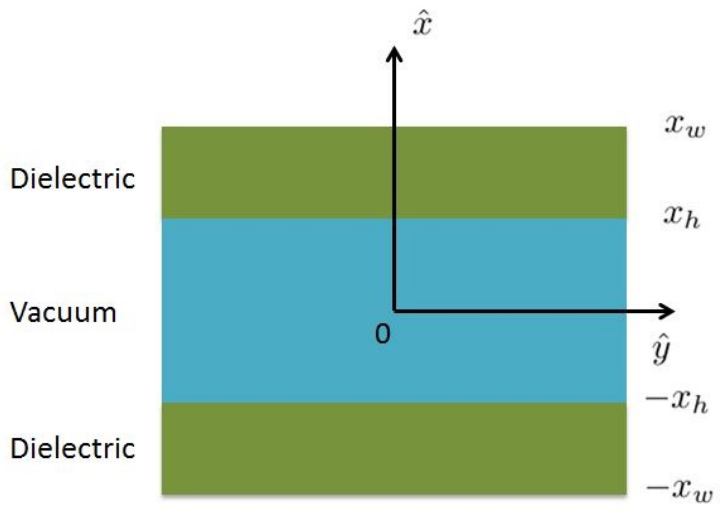

Figure A.1: Simple geometry of structure without the vanes

that conducting vanes are embedded in the dielectrics for $(x_w > |x| > x_v)$. The vanes are modeled by setting the parallel component of the electric field to zero at their boundaries, $E_z(\pm x_v) = 0$. The perpendicular component of the field is unaffected.

We proceed to write Maxwell's equations, which are fundamental in describing electromagnetic waves. For a more detailed explanation, the reader can refer to [19] or [20].

$$\nabla \times \vec{H} = \vec{J} + \epsilon \frac{\partial \vec{E}}{\partial t},$$

$$\nabla \times \vec{E} = -\mu \frac{\partial \vec{H}}{\partial t}.$$

We then separate the gradient operator $\nabla = \nabla_t + \nabla_z$, where

$$\nabla_t = \frac{\partial}{\partial x} + \frac{\partial}{\partial y},$$

$$\nabla_z = \frac{\partial}{\partial z}.$$

Current exists on the surface of the sheath, where conducting slabs run along the structure

$$\vec{J} = \vec{J_s^+}\delta(x - x_h) + \vec{J_s^-}\delta(x + x_h)$$

The surface currents can be decomposed into y and z components:

$$\vec{J_s^+} = \vec{J_{sy}^+} + \vec{J_{sz}^+},$$

and

$$\vec{J_s^-} = \vec{J_{sy}^-} + \vec{J_{sz}^-}.$$

Since fields propagate with phase $e^{i(k_z z + k_y y - \omega t)}$, Maxwell's equations result in:

$$i\omega\epsilon\vec{E} = -\nabla_t \times \vec{H} - ik_z\hat{z} \times \vec{H},$$

$$i\omega\mu\vec{H} = \nabla_t \times \vec{H} + ik_z\hat{z} \times \vec{H},$$

On the transverse plane, we have:

$$i\omega\epsilon\vec{E_t} = -\nabla_t \times \vec{H_z} - ik_z\hat{z} \times \vec{H_t}, \tag{A.1}$$

$$i\omega\mu\vec{H_t} = \nabla_t \times \vec{E_z} + ik_z\hat{z} \times \vec{E_t}. \tag{A.2}$$

Perform cross product on both sides of equations (A.1) and (A.2) with $\hat{z}\times$

$$i\omega\epsilon\hat{z} \times \vec{E_t} = -\nabla_t\vec{H_z} + ik_z\vec{H_t}, \tag{A.3}$$

and

$$i\omega\mu\hat{z} \times \vec{H_t} = \nabla_t\vec{E_z} - ik_z\vec{E_t}. \tag{A.4}$$

We assume non-magnetic material throughout, $\mu = \mu_o$. We define a quantity γ such that:

$$\gamma^2 = k_z^2 - \omega^2\mu\epsilon = k_z^2 - \epsilon_r\frac{\omega^2}{c^2}$$

Combining (A.1) and (A.4), (A.2) and (A.3), we have:

$$\vec{E}_t = \frac{1}{\gamma^2}\left(-i\omega\mu\nabla_t \times \vec{H}_z - ik_z\nabla_t\vec{E}_z\right), \tag{A.5}$$

and

$$\vec{H}_t = \frac{1}{\gamma^2}\left(i\omega\epsilon\nabla_t \times \vec{E}_z + ik_z\nabla_t\vec{H}_z\right). \tag{A.6}$$

On $\hat{y}$, the long transverse direction, (A.5) and (A.6) take the form

$$E_y = \frac{1}{\gamma^2}\left(i\omega\mu\frac{\partial H_z}{\partial x} + k_z k_y E_z\right), \tag{A.7}$$

and

$$H_y = \frac{1}{\gamma^2}\left(-i\omega\epsilon\frac{\partial E_z}{\partial x} + k_z k_y H_z\right). \tag{A.8}$$

Here, (A.7) and (A.8) serve to define the relation between the transverse and longitudinal fields. The task at hand is to determine the boundary conditions across different regions.

A.1.2 Boundary conditions:

Electromagnetic field theory dictates that the electric field tangent to conducting walls vanishes. As mentioned, we replace this by the conditions $E_z(\pm x_v) = 0$ and $E_y(\pm x_w)$. The conditions at the conducting sheaths will be considered separately.

We define vectors $\vec{t}$ to run tangent to the sheaths at $x = \pm x_h$. These vectors are on the $y - z$ plane, $\vec{t_\pm} = \hat{z}t_{z\pm} + \hat{y}t_{y\pm}$. The pitch of each sheaths can be related to $\vec{t_\pm}$. The boundary condition for the electric field requires its component tangent to the sheaths to vanish. Or in other words, $\vec{t_\pm}.\vec{E}(\pm x_h) = 0$. The pitch α defined before can be related as:

$$\frac{t_z^+}{t_y^+} = \alpha, \qquad \text{and} \qquad \frac{t_z^-}{t_y^-} = -\alpha.$$

which results in

$$\frac{E_y(x_h)}{E_z(x_h)} = -\alpha, \qquad \text{and} \qquad \frac{E_y(-x_h)}{E_z(-x_h)} = \alpha.$$

From now on, we denote $(+)$ for the top boundary and $(-)$ for the bottom boundary, which translates to

$$\frac{E_y^+}{E_z^+} = -\alpha, \qquad \text{and} \qquad \frac{E_y^-}{E_z^-} = \alpha. \tag{A.9}$$

Current runs along the conducting sheaths. From Maxwell's equations, we arrive at the boundary conditions for $\vec{J}$:

$$J_{sz}^+ = H_y(x_h^+) - H_y(x_h^-) \equiv H_y^{++} - H_y^{+-},$$

$$J_{sz}^- = H_y(-x_h^+) - H_y(-x_h^-) \equiv H_y^{-+} - H_y^{--},$$

$$J_{sy}^+ = -H_z(x_h^+) + H_z(x_h^-) \equiv -H_z^{++} + H_z^{+-},$$

and

$$J_{sy}^- = -H_z(-x_h^+) + H_z(-x_h^-) \equiv -H_z^{-+} + H_z^{--}.$$

where the first sign in the sequence represents top/bottom boundary and the latter represents the side that the term represents. For example, $^{+-}$ means below the upper boundary. Note that $\vec{J}$ is directed along the sheaths, so it can be represented by the vector $\vec{t}$ defined above. Specifically,

$$\frac{J_{sz^+}}{J_{sy^+}} = \alpha, \qquad \text{and} \qquad \frac{J_{sz^-}}{J_{sy^-}} = -\alpha.$$

The boundary conditions on the magnetic fields are then derived from the relations above as

$$H_y^{++} + \alpha H_z^{++} = H_y^{+-} + \alpha H_z^{+-}, \tag{A.10}$$

and

$$H_y^{--} - \alpha H_z^{--} = H_y^{-+} - \alpha H_z^{-+}. \tag{A.11}$$

A.1.3 Field Equations:

From Maxwell's equations, a general wave equation can be derived. For a formal treatment, the reader can refer to [19] or [17]. We define a quantity ψ^2 such that:

$$\psi^2 = k_z^2 + k_y^2 - \omega^2\mu\epsilon = k_y^2 + \gamma^2$$

The waves equations for the longitudinal fields are then

$$\left(\frac{\partial^2}{\partial x^2} - \psi^2\right) E_z = 0, \qquad \text{and} \qquad \left(\frac{\partial^2}{\partial x^2} - \psi^2\right) H_z = 0. \tag{A.12}$$

a) In the Top Dielectric:

The boundary conditions for fields in this region include $E_z(x_v) = 0$ and $E_y(x_w) = 0$, which implies $\frac{\partial H_z}{\partial x}(x_w) = 0$.

In general, the phase velocity is less than the speed of light, $\psi^2 > 0$, so the longitudinal field solutions in this region take the form

$$E_z(x) = E_z^{+} \frac{sinh\psi(x_v - x)}{sinh\psi(x_v - x_h)},$$

$$H_z(x) = H_z^{++} \frac{cosh\psi(x_v - x)}{cosh\psi(x_w - x_h)}.$$

It is easier to examine the equations when we introduce the following:

$$T_w = tanh\psi(x_w - x_h),$$

$$T_v = tanh\psi(x_v - x_h),$$

and

$$T_o = tanh\psi_o x_h.$$

where the subscript "$_o$" means free space parameters are used.

From (A.7) and (A.9), the magnetic field amplitude at boundary x_h relates to the electric field amplitude at x_h as

$$H_z^{++} = \frac{\alpha\gamma^2 + k_z k_y}{i\omega\mu T_w \psi} E_z^+. \tag{A.13}$$

From (A.8) and (A.13) the transverse magnetic field at the boundary for this region is then

$$H_y^{++} = E_z^+ \frac{i\omega\epsilon\psi}{\gamma^2} \left[\frac{1}{T_v} - k_z k_y \frac{\alpha\gamma^2 + k_z k_y}{\omega^2\mu\epsilon\psi^2 T_w} \right]. \tag{A.14}$$

b) In the Bottom Dielectric:

Similarly, the field solutions take the form

$$E_z(x) = E_z^- \frac{sinh\psi(x_v + x)}{sinh\psi(x_v - x_h)},$$

and

$$H_z(x) = H_z^{--} \frac{cosh\psi(x_v + x)}{cosh\psi(x_w - x_h)}.$$

From (A.7), we get

$$H_z^{--} = \frac{\alpha\gamma^2 - k_z k_y}{i\omega\mu T_w \psi} E_z^-. \tag{A.15}$$

From (A.8) and (A.15), we find:

$$H_y^{--} = -E_z^- \frac{i\omega\epsilon\psi}{\gamma^2} \left[\frac{1}{T_v} + k_z k_y \frac{\alpha\gamma^2 - k_z k_y}{\omega^2\mu\epsilon\psi^2 T_w} \right]. \tag{A.16}$$

c) Vacuum region between the sheaths:

The general solutions are superpositions of even and odd functions:

$$E_z(x) = E_s sinh\psi_o x + E_c cosh\psi_o x,$$

and

$$H_z(x) = H_s sinh\psi_o x + H_c cosh\psi_o x.$$

At the sheath boundaries, we have:

$$E_z(x_h) = E_s sinh\psi_o x_h + E_c cosh\psi_o x_h,$$

and

$$E_z(x) = -E_s sinh\psi_o x_h + E_c cosh\psi_o x_h.$$

Thus we can write:

$$E_c = \frac{E_z^+ + E_z^-}{2cosh\psi_o x_h}, \qquad \text{and} \qquad Es = \frac{E_z^+ - E_z^-}{2sinh\psi_o x_h}. \tag{A.17}$$

From (A.7),(A.9), and (A.17) at $x = x_h$, top boundary, we have:

$$H_z^{+-} \equiv H_z(x_h^-) = H_s sinh\psi_o x_h + H_c cosh\psi_o x_h = -E_z^+ \frac{\alpha\gamma_o^2 + k_z k_y}{i\omega\mu\psi_o}, \tag{A.18}$$

and at $x = -x_h$, bottom boundary, we have:

$$H_z^{-+} \equiv H_z(-x_h^+) = -H_s sinh\psi_o x_h + H_c cosh\psi_o x_h = E_z^- \frac{\alpha\gamma_o^2 - k_z k_y}{i\omega\mu\psi_o}. \tag{A.19}$$

From (A.18) and (A.19):

$$H_s = \frac{1}{2i\omega\mu\psi_o cosh\psi_o x_h} \left[-(\alpha\gamma_o^2 + k_z k_y)E_z^+ + (\alpha\gamma_o^2 - k_z k_y)E_z^- \right],$$

and

$$H_c = \frac{1}{2i\omega\mu\psi_o sish\psi_o x_h}\left[-(\alpha\gamma_o^2 + k_z k_y)E_z^+ - (\alpha\gamma_o^2 - k_z k_y)E_z^-\right].$$

The magnetic field on the upper and lower sheaths can be expressed by replacing H_s and H_c into the general solutions:

$$H_z^{+-} = -\frac{1}{2i\omega\mu\psi_o}\left[\left(T_o + \frac{1}{T_o}\right)(\alpha\gamma_o^2 + k_z k_y)E_z^+ - \left(T_o - \frac{1}{T_o}\right)(\alpha\gamma_o^2 - k_z k_y)E_z^-\right], \tag{A.20}$$

and

$$H_z^{+-} = \frac{1}{2i\omega\mu\psi_o}\left[\left(T_o - \frac{1}{T_o}\right)(\alpha\gamma_o^2 + k_z k_y)E_z^+ - \left(T_o + \frac{1}{T_o}\right)(\alpha\gamma_o^2 - k_z k_y)E_z^-\right]. \tag{A.21}$$

We can then proceed to find the transverse magnetic field solutions by referring to (A.8). First, we write down the spatial derivative of E_z at the boundaries:

$$\frac{\partial E_z}{\partial x}(x = x_h) = \frac{\psi_o}{2}\left(T_o + \frac{1}{T_o}\right)E_z^+ + \frac{\psi_o}{2}\left(T_o - \frac{1}{T_o}\right)E_z^-,$$

and

$$\frac{\partial E_z}{\partial x}(x = x_h) = -\frac{\psi_o}{2}\left(T_o - \frac{1}{T_o}\right)E_z^+ - \frac{\psi_o}{2}\left(T_o + \frac{1}{T_o}\right)E_z^-.$$

Combining these expressions together with H_z solutions found above in (A.20) and (A.21) with (A.8), we have:

$$\begin{aligned} H_y^{+-} = -\frac{i\omega\epsilon_o\psi_o}{2\gamma_o^2}\Bigg[&E_z^+\left(T_o + \frac{1}{T_o}\right)\left(1 - k_z k_y\frac{\alpha\gamma_o^2 + k_z k_y}{\omega^2\mu_o\epsilon_o\psi_o^2}\right) \\ &+E_z^-\left(T_o - \frac{1}{T_o}\right)\left(1 + k_z k_y\frac{\alpha\gamma_o^2 - k_z k_y}{\omega^2\mu_o\epsilon_o\psi_o^2}\right)\Bigg], \end{aligned} \tag{A.22}$$

and

$$\begin{aligned} H_y^{-+} = &\, i\omega\epsilon_o\psi_o E_z^+\left(T_o - \frac{1}{T_o}\right)\left(1 - k_z k_y\frac{\alpha\gamma_o^2 + k_z k_y}{\omega^2\mu_o\epsilon_o\psi_o^2}\right) \\ &+\frac{i\omega\epsilon_o\psi_o}{2\gamma_o^2}E_z^-\left(T_o + \frac{1}{T_o}\right)\left(1 + k_z k_y\frac{\alpha\gamma_o^2 - k_z k_y}{\omega^2\mu_o\epsilon_o}\right). \end{aligned} \tag{A.23}$$

A.1.4 Dispersion Relation:

From the boundary conditions (A.10), (A.11), and the magnetic field solutions in the top dielectric (A.13), (A.14), the bottom dielectric (A.15), (A.16), the vacuum region between the sheaths (A.20), (A.21), (A.22), (A.23), we can derive the dispersion equation for the planar structure. Again, non-magnetic material is assumed, and $\mu = \mu_o$.

At x_h^+, in top dielectric:

$$\frac{H_y^{++}}{\alpha} + H_z^{++} = \frac{i\omega\epsilon\psi}{\alpha\gamma^2}\left[\frac{1}{T_v} - \frac{\left(\alpha\gamma^2 + k_z k_y\right)^2}{\omega^2\mu\epsilon\psi^2 T_w}\right] E_z^+ \equiv B_{++} E_z^+. \tag{A.24}$$

At $-x_h^-$, in bottom dielectric:

$$\frac{H_y^{--}}{\alpha} - H_z^{--} = -\frac{i\omega\epsilon\psi}{\alpha\gamma^2}\left[\frac{1}{T_v} - \frac{\left(\alpha\gamma^2 - k_z k_y\right)^2}{\omega^2\mu\epsilon\psi^2 T_w}\right] E_z^- \equiv -B_{--} E_z^-. \tag{A.25}$$

At x_h^-, in vacuum region at the top boundary:

$$\begin{aligned}\frac{H_y^{+-}}{\alpha} + H_z^{+-} = -\frac{i\omega\epsilon_o\psi_o}{2\alpha\gamma_o^2}\Bigg\{ & E_z^+\left(T_o + \frac{1}{T_o}\right)\left[1 - \frac{\left(\alpha\gamma_o^2 + k_z k_y\right)^2}{\omega^2\mu\epsilon_o\psi_o^2}\right] \\ & + E_z^-\left(T_o - \frac{1}{T_o}\right)\left[1 + \frac{\left(\alpha\gamma_o^2\right)^2 - k_z^2 k_y^2}{\omega^2\mu\epsilon_o\psi_o^2}\right]\Bigg\} \\ & \equiv -\left(B_{o+} E_z^+ + B_\times E_z^-\right).\end{aligned} \tag{A.26}$$

At $-x_h^+$, in vacuum region at the bottom boundary:

$$\begin{aligned}\frac{H_y^{-+}}{\alpha} - H_z^{-+} = \frac{i\omega\epsilon_o\psi_o}{2\alpha\gamma_o^2}\Bigg\{ & E_z^+\left(T_o - \frac{1}{T_o}\right)\left[1 + \frac{\left(\alpha\gamma_o^2\right)^2 - k_z^2 k_y^2}{\omega^2\mu\epsilon_o\psi_o^2}\right] \\ & + E_z^-\left(T_o + \frac{1}{T_o}\right)\left[1 - \frac{\left(\alpha\gamma_o^2 - k_z k_y\right)^2}{\omega^2\mu\epsilon_o\psi_o^2}\right]\Bigg\} \\ & \equiv B_\times E_z^+ + B_{o-} E_z^-.\end{aligned} \tag{A.27}$$

Matching (A.24) with (A.26) as in (A.10), and (A.25) with (A.27) as in (A.11), we have the dispersion equation for the structure:

$$(B_{++} + B_{o+})(B_{--} + B_{o-}) = B_{\times}^2. \tag{A.28}$$

The simplified terms are:

$$\begin{aligned}
B_{++} &= \frac{\epsilon_r \psi}{\gamma^2}\left[\frac{1}{T_v} - \frac{(\alpha\gamma^2 + k_z k_y)^2}{\omega^2 \mu \epsilon \psi^2 T_w}\right], \\
B_{--} &= \frac{\epsilon_r \psi}{\gamma^2}\left[\frac{1}{T_v} - \frac{(\alpha\gamma^2 - k_z k_y)^2}{\omega^2 \mu \epsilon \psi^2 T_w}\right], \\
B_{o+} &= \frac{\psi_o}{2\gamma_o^2}\left(T_o + \frac{1}{T_o}\right)\left[1 - \frac{(\alpha\gamma_o^2 + k_z k_y)^2}{\omega^2 \mu \epsilon_o \psi_o^2}\right], \\
B_{o-} &= \frac{\psi_o}{2\gamma_o^2}\left(T_o + \frac{1}{T_o}\right)\left[1 - \frac{(\alpha\gamma_o^2 - k_z k_y)^2}{\omega^2 \mu \epsilon_o \psi_o^2}\right], \\
\text{and} \quad B_{\times} &= \frac{\psi_o}{2\gamma_o^2}\left(T_o - \frac{1}{T_o}\right)\left[1 + \frac{(\alpha\gamma_o^2)^2 - k_z^2 k_y^2}{\omega^2 \mu \epsilon_o \psi_o^2}\right].
\end{aligned}$$

A.1.5 Simple Model

When $k_y = 0$, $\psi = \gamma$, waves propagate between the sheaths either as odd mode ($\propto sinh$) or even mode ($\propto cosh$). This phenomenon arises from the relation between transverse mode and longitudinal mode (A.7) and (A.8). The dispersion is now:

$$B_{++} + B_{o+} = \pm B_{\times}. \tag{A.29}$$

where the $(+)$ and $(-)$ signs in front of $B_\times$ represent odd and even mode respectively.

The reduced terms are:

$$
\begin{aligned}
B_{++} &= B_{--} = \frac{i\omega\epsilon}{\alpha\gamma}\left[\frac{1}{T_v} - \frac{\alpha^2\gamma^2}{\omega^2\mu\epsilon T_w}\right], \\
B_{o+} &= B_{o-} = \frac{i\omega\epsilon_o}{2\alpha\gamma_o}\left(T_o + \frac{1}{T_o}\right)\left[1 - \frac{\alpha^2\gamma_o^2}{\omega^2\mu\epsilon_o}\right], \\
\text{and} \qquad B_\times &= \frac{i\omega\epsilon_o}{2\alpha\gamma_o}\left(T_o - \frac{1}{T_o}\right)\left[1 + \frac{\alpha^2\gamma_o^2}{\omega^2\mu\epsilon_o}\right].
\end{aligned}
$$

A.2 Pierce Impedance

The Pierce impedance is a quantity of interest for characterizing the coupling strength between the electron beam and the electromagnetic wave. In SI units, it is defined as

$$Z_p = \frac{|E_z(x=0)|^2}{2k_z^2 P}, \tag{A.30}$$

where

$$P \equiv Power flux = Re\left[\int_S dxdy\hat{z}.(\vec{E} \times \vec{H}^*)\right], \tag{A.31}$$

and the surface S defines the cross section of the structure.

A.2.1 Matrix Formulation of Dispersion

Dispersion relation can be derived via manipulating matrices, specifically admittance matrices. It is analogous to wave mechanics vs matrix formalism in quantum mechanics. Working with wave equations gives us a good intuition of the modes of the system, but putting up matrices provides an easier analytic and computational strategy. Moreover, the matrices derived can be used to formulate Pierce impedance.

First, define the admittance terms via the boundary conditions from A.1.2:

$$J_{sz}^+ = H_y^{++} - H_y^{+-} = Y_z^{11} E_z^+ + Y_z^{12} Ez^-,$$

$$J_{sz}^- = H_y^{-+} - H_y^{--} = Y_z^{21} E_z^+ + Y_z^{22} Ez^-,$$

$$J_{sy}^+ = -H_z^{++} + H_z^{+-} = Y_y^{11} E_y^+ + Y_y^{12} Ey^-,$$

$$J_{sy}^- = -H_z^{-+} + H_z^{--} = Y_y^{21} E_y^+ + Y_y^{22} Ey^-.$$

In matrix form:

$$\begin{pmatrix} J_{sz}^{+} \\ \\ J_{sz}^{-} \end{pmatrix} = \begin{pmatrix} Y_z^{11} & Y_z^{12} \\ \\ Y_z^{21} & Y_z^{22} \end{pmatrix} \begin{pmatrix} E_z^{+} \\ \\ E_z^{-} \end{pmatrix} \equiv \overline{\overline{Y_z}} \begin{pmatrix} E_z^{+} \\ \\ E_z^{-} \end{pmatrix}, \tag{A.32}$$

and

$$\begin{pmatrix} J_{sy}^{+} \\ \\ J_{sy}^{-} \end{pmatrix} = \begin{pmatrix} Y_y^{11} & Y_y^{12} \\ \\ Y_y^{21} & Y_y^{22} \end{pmatrix} \begin{pmatrix} E_y^{+} \\ \\ E_y^{-} \end{pmatrix} \equiv \overline{\overline{Y_y}} \begin{pmatrix} E_y^{+} \\ \\ E_y^{-} \end{pmatrix}. \tag{A.33}$$

The matrices' admittance entries can be found by plugging in magnetic field solutions from A.1.3:

$$\begin{aligned} Y_z^{11} =& \frac{i\omega\epsilon\psi}{\gamma^2}\left[\frac{1}{T_v} - k_z k_y \frac{\alpha\gamma^2 + k_z k_y}{\omega^2\mu\epsilon\psi^2 T_w}\right] \\ &+ \frac{i\omega\epsilon_o\psi_o}{2\gamma_o^2}\left(T_o + \frac{1}{T_o}\right)\left[1 - k_z k_y \frac{\alpha\gamma^2 + k_z k_y}{\omega^2\mu\epsilon_o\psi_o^2}\right], \end{aligned} \tag{A.34}$$

$$Y_z^{12} = \frac{i\omega\epsilon_o\psi_o}{2\gamma_o^2}\left(T_o - \frac{1}{T_o}\right)\left[1 + k_z k_y \frac{\alpha\gamma^2 - k_z k_y}{\omega^2\mu\epsilon_o\psi_o^2}\right], \tag{A.35}$$

$$Y_z^{21} = \frac{i\omega\epsilon_o\psi_o}{2\gamma_o^2}\left(T_o - \frac{1}{T_o}\right)\left[1 - k_z k_y \frac{\alpha\gamma^2 + k_z k_y}{\omega^2\mu\epsilon_o\psi_o^2}\right], \tag{A.36}$$

$$\begin{aligned} Y_z^{22} =& \frac{i\omega\epsilon\psi}{\gamma^2}\left[\frac{1}{T_v} + k_z k_y \frac{\alpha\gamma^2 - k_z k_y}{\omega^2\mu\epsilon\psi^2 T_w}\right] \\ &+ \frac{i\omega\epsilon_o\psi_o}{2\gamma_o^2}\left(T_o + \frac{1}{T_o}\right)\left[1 + k_z k_y \frac{\alpha\gamma^2 - k_z k_y}{\omega^2\mu\epsilon_o\psi_o^2}\right], \end{aligned} \tag{A.37}$$

$$Y_y^{11} = \frac{\alpha\gamma^2 + k_z k_y}{i\omega\mu\psi T_w\alpha} + \left(T_o + \frac{1}{T_o}\right)\frac{\alpha\gamma_o^2 + k_z k_y}{2i\omega\mu\psi_o\alpha}, \tag{A.38}$$

$$Y_y^{12} = \left(T_o - \frac{1}{T_o}\right)\frac{\alpha\gamma_o^2 - k_z k_y}{2i\omega\mu\psi_o\alpha}, \tag{A.39}$$

$$Y_y^{21} = \left(T_o - \frac{1}{T_o}\right)\frac{\alpha\gamma_o^2 + k_z k_y}{2i\omega\mu\psi_o\alpha}, \tag{A.40}$$

$$Y_y^{22} = \frac{\alpha\gamma^2 - k_z k_y}{i\omega\mu\psi T_w\alpha} + \left(T_o + \frac{1}{T_o}\right)\frac{\alpha\gamma_o^2 - k_z k_y}{2i\omega\mu\psi_o\alpha}. \tag{A.41}$$

The boundary conditions for surface current densities in matrix notation can be written as:

$$\begin{pmatrix} J_{sz}^{+} \\ \\ J_{sz}^{-} \end{pmatrix} = \begin{pmatrix} \alpha & 0 \\ \\ 0 & -\alpha \end{pmatrix} \begin{pmatrix} J_{sy}^{+} \\ \\ J_{sy}^{+} \end{pmatrix}, \tag{A.42}$$

which, with relations (A.32) and (A.33), is equivalent to:

$$\overline{\overline{Y_z}} \begin{pmatrix} E_z^{+} \\ \\ E_z^{+} \end{pmatrix} = \alpha \begin{pmatrix} 1 & 0 \\ \\ 0 & -1 \end{pmatrix} \overline{\overline{Y_y}} \begin{pmatrix} E_y^{+} \\ \\ E_y^{+} \end{pmatrix}. \tag{A.43}$$

The boundary condition for electric fields (A.9) in matrix notation is:

$$\begin{pmatrix} E_y^{+} \\ \\ E_y^{-} \end{pmatrix} = \alpha \begin{pmatrix} -1 & 0 \\ \\ 0 & 1 \end{pmatrix} \begin{pmatrix} E_z^{+} \\ \\ E_z^{+} \end{pmatrix}. \tag{A.44}$$

Combining (A.43) and (A.44), the dispersion relation can be written in matrix notation as:

$$\overline{\overline{Y_z}} = \alpha^2 \begin{pmatrix} 1 & 0 \\ \\ 0 & -1 \end{pmatrix} \overline{\overline{Y_y}} \begin{pmatrix} -1 & 0 \\ \\ 0 & 1 \end{pmatrix} \tag{A.45}$$

Both forms of the dispersion relation are valid and can be used to cross check each other. The previous derivation is preferable for determining propagation modes inside the structure while the matrix notation with its admittance matrices is predominantly used in formulating Pierce impedance for those modes.

A.2.2 Power Flux

Linear perturbation technique can be applied to Maxwell's equations to determine the power flux in (A.31). Let $\vec{E} = \vec{E_o} + \delta\vec{E}$,$\vec{H} = \vec{H_o} + \delta\vec{H}$ and $k = k_o + \delta k$ where δ represents a small linear perturbation. Maxwell's equations can be linearized as:

$$-i\omega\epsilon\delta\vec{E} = \nabla_t \times \delta\vec{H} + ik_o\hat{z} \times \delta\vec{H} + i\delta k\hat{z} \times \vec{H_o}, \tag{A.46}$$

$$\omega\mu\delta\vec{H} = \nabla_t \times \delta\vec{E} + ik_o\hat{z} \times \delta\vec{E} + i\delta k\hat{z} \times \vec{E_o}. \tag{A.47}$$

We multiply and integrate:

$$\int_S (A.46).\vec{E_o^*}dS,$$
$$\int_S (A.47).\vec{H_o^*}dS.$$

After some algebra, we have the equivalent equations:

$$\begin{aligned} -i\omega\epsilon \int d^2x\, \vec{E_o^*}.\delta\vec{E} &= -i\omega\mu \int d^2x\, \delta\vec{H}.\vec{H_o^*} + i\delta k \int d^2x\, \vec{E_o^*}.\hat{z} \times \vec{H_o}, \\ i\omega\mu \int d^2x\, \vec{H_o^*}.\delta\vec{H} &= i\omega\epsilon \int d^2x\, \delta\vec{E}.\vec{E_o^*} + i\delta k \int d^2x\, \vec{H_o^*}.\hat{z} \times \vec{E_o} \\ &\quad + \int d^2x\, \delta\vec{E}.\vec{J_{so}^*}. \end{aligned}$$

Combining these equations gives:

$$i\delta k \int d^2x\, \hat{z}.\left(\vec{E_o} \times \vec{H_o^*} + \vec{E_o^*} \times \vec{H_o}\right) + \int d^2x\, \delta\vec{E}.\vec{J_{so}^*} = 0.$$

From (A.31), the equation above is equivalent to:

$$2i\delta kP = -\int d^2x\, \delta\vec{E}.\vec{J_{so}^*}. \tag{A.48}$$

Equation (A.48) fundamentally establishes the relation between power flux in longitudinal direction and surface current.

A.2.3 Pierce Impedance Formulation

The linear electric field perturbations can be referred from (A.32) and (A.33). Define $\overline{\overline{Z_z}} = \overline{\overline{Y_z}}^{-1}$ and $\overline{\overline{Z_y}} = \overline{\overline{Y_y}}^{-1}$, we have:

$$\begin{pmatrix} \delta E_z^+ \\ \\ \delta E_z^- \end{pmatrix} = \overline{\overline{\delta Z_z}} \begin{pmatrix} J_{sz}^+ \\ \\ J_{sz}^- \end{pmatrix} \qquad \text{and} \qquad \begin{pmatrix} \delta E_y^+ \\ \\ \delta E_y^- \end{pmatrix} = \overline{\overline{\delta Z_y}} \begin{pmatrix} J_{sy}^+ \\ \\ J_{sy}^- \end{pmatrix}$$

Relation (A.48) in matrix and tensor notation can be interpreted as

$$\begin{aligned} P =& \frac{i}{2} \int d^2x \overline{\frac{\delta E}{\delta k}} \overline{J_s^*} \\ =& \frac{iL_y}{2} \sum_i \overline{\frac{dE_i}{dk}} \overline{J_{si}^*}. \end{aligned}$$

$$\Leftrightarrow \qquad P = \frac{iL_y}{2} \left\{ \begin{pmatrix} J_{sz}^{+*} & J_{sz}^{-*} \end{pmatrix} \frac{d\overline{\overline{Z_z}}}{dk_z} \begin{pmatrix} J_{sz}^+ \\ \\ J_{sz}^- \end{pmatrix} + \begin{pmatrix} J_{sy}^{+*} & J_{sy}^{-*} \end{pmatrix} \frac{d\overline{\overline{Z_y}}}{dk_z} \begin{pmatrix} J_{sy}^+ \\ \\ J_{sy}^- \end{pmatrix} \right\}.$$

With boundary condition (A.42), we have the equation for power flux as

$$P = \frac{iL_y}{2} \overline{J_{sz}}^* \left\{ \frac{d\overline{\overline{Z_z}}}{dk_z} + \frac{1}{\alpha^2} \begin{pmatrix} 1 & 0 \\ \\ 0 & -1 \end{pmatrix} \frac{d\overline{\overline{Z_y}}}{dk_z} \begin{pmatrix} 1 & 0 \\ \\ 0 & -1 \end{pmatrix} \right\} \overline{J_{sz}}. \tag{A.49}$$

Again, $\overline{J_{sz}} = \begin{pmatrix} J_{sz}^+ \\ \\ J_{sz}^- \end{pmatrix} = \overline{\overline{Y_z}}\, \overline{E_z}$ and $\overline{J_{sz}}^* = \begin{pmatrix} J_{sz}^{+*} & J_{sz}^{-*} \end{pmatrix} = \overline{E_z}^*\, \overline{\overline{Y_z}}^\dagger$.

In (A.30), we can write

$$E_z(x=0) = \frac{E_z^+ + E_z^-}{2cosh\psi_o x_h},$$

and define a ratio between E_z^+ and E_z^- as

$$R = \frac{E_z^-}{E_z^+}.$$

The formula for Pierce impedance that we can use is then:

$$Z_p = |1+R|^2 / \, 4ik_z^2 cosh^2\psi_o x_h L_y \begin{pmatrix} 1 & R \end{pmatrix} \overline{\overline{Y_z}}^{\dagger} \left\{ \frac{d\overline{\overline{Z_z}}}{dk_z} + \frac{1}{\alpha^2} \begin{pmatrix} 1 & 0 \\ 0 & -1 \end{pmatrix} \frac{d\overline{\overline{Z_y}}}{dk_z} \begin{pmatrix} 1 & 0 \\ 0 & -1 \end{pmatrix} \right\} \overline{\overline{Y_z}} \begin{pmatrix} 1 \\ R \end{pmatrix}. \tag{A.50}$$

Denote frequently used matrix $\begin{pmatrix} 1 & 0 \\ 0 & -1 \end{pmatrix}$ as $\overline{\overline{\sigma}}$ and $\begin{pmatrix} 1 \\ R \end{pmatrix}$ as $\overline{\eta}$, the final and convenient form of Z_p can be written as:

$$Z_p = \frac{|1+R|^2}{4ik_z^2 cosh^2\psi_o x_h L_y \overline{\eta}^{\dagger} \overline{\overline{Y_z}}^{\dagger} \left\{ \frac{d\overline{\overline{Z_z}}}{dk_z} + \frac{1}{\alpha^2} \overline{\overline{\sigma}} \frac{d\overline{\overline{Z_y}}}{dk_z} \overline{\overline{\sigma}} \right\} \overline{\overline{Y_z}} \overline{\eta}}. \tag{A.51}$$

A.3 Gain Analysis

For a more rigorous treatment of gain analysis, the reader can refer to [18]. The formulation provided here is partially based on [18] and [17].

A.3.1 Adding Beam Current

Let $\vec{k_s}$ be the wavevector for structure without beam: $\vec{k_s} = k_{sz}\hat{z} + k_{sy}\hat{y}$

Let $\vec{e}$ and $\vec{h}$ be the basis vectors for our modes.

From Maxwell's equations, we have:

$$
\begin{aligned}
i\omega\mu\vec{h} &= \frac{d}{dx}\hat{x} \times \vec{e} + i\vec{k_s} \times \vec{e}, \\
-i\omega\mu\vec{h^*} &= \frac{d}{dx}\hat{x} \times \vec{e^*} - i\vec{k_s} \times \vec{e^*}, \\
-i\omega\epsilon\vec{e} &= \frac{d}{dx}\hat{x} \times \vec{h} + i\vec{k_s} \times \vec{h},
\end{aligned}
$$

and

$$
i\omega\epsilon\vec{e^*} = \frac{d}{dx}\hat{x} \times \vec{h^*} - i\vec{k_s} \times \vec{h^*}.
$$

Add beam current $\vec{J_b}$. We define $\vec{E} = A\vec{e}$ and $\vec{H} = A\vec{h}$.

$$
i\omega\mu\vec{H} = \frac{d}{dx}\hat{x} \times \vec{E} + i\vec{k} \times \vec{E}, \tag{A.52}
$$

and

$$
\vec{J_b} - i\omega\epsilon\vec{E} = \frac{d}{dx}\hat{x} \times \vec{H} + i\vec{k} \times \vec{H}. \tag{A.53}
$$

We dot (A.52) with $\vec{h^*}$ and integrate from $-x_w$ to x_w. After some algebra, we have:

$$i\omega\mu \int_{-x_w}^{x_w} dx\vec{H}.\vec{h^*} - i\omega\epsilon \int_{-x_w}^{x_w} dx\vec{E}.\vec{e^*} = \vec{e^*}.\hat{x} \times \vec{H} \Big|_{-x_w \to x_w} + i\left(\vec{k} - \vec{k_s}\right) \int_{-x_w}^{x_w} dx\vec{E} \times \vec{h^*}. \tag{A.54}$$

Similarly, we dot (A.53) with $\vec{e^*}$ and integrate from $-x_w$ to x_w:

$$\int_{-x_w}^{x_w} dx\vec{e^*}.\vec{J_b} - i\omega\epsilon \int_{-x_w}^{x_w} dx\vec{E}.\vec{e^*} + i\omega\mu \int_{-x_w}^{x_w} dx\vec{H}.\vec{h^*} = \vec{e^*}.\hat{x}\times\vec{H} \Big|_{-x_w \to x_w} + i\left(\vec{k} - \vec{k_s}\right) \int_{-x_w}^{x_w} dx\vec{H}\times\vec{e^*}. \tag{A.55}$$

We subtract (A.54) from (A.55), assuming surface terms are zero:

$$\int_{-x_w}^{x_w} dx\vec{J_b}.\vec{e^*} = i\left(\vec{k} - \vec{k_s}\right) \int_{-x_w}^{x_w} dx \left(\vec{H} \times \vec{e^*} + \vec{h^*} \times \vec{E}\right).$$

$\vec{J_b}$ varries with phase $\phi = kz - wt$. Let $\vec{J_{bz}} = u(x)\,(I_{bo})\left\langle e^{-i\phi}\right\rangle$. We have:

$$A\left(\vec{k} - \vec{k_s}\right).\vec{P} = iI_{bo}\left\langle e^{-i\phi}\right\rangle \vec{e_z^*}, \tag{A.56}$$

where $P = 4\int_{-x_w}^{x_w} dx \left(\vec{e} \times \vec{h^*} + \vec{e^*} \times \vec{h}\right)$.

A.3.2 Equation of Motion

Again, we define wave phase as $\phi = kz - wt$, then:

$$\frac{d\phi}{dz} = k - \omega\frac{dt}{dz} = k - \frac{\omega}{v_z} \equiv k - k_v,$$

and

$$\frac{d^2\phi}{dz^2} = \frac{\omega}{v_z^2}\frac{dv_z}{dz}.$$

In non-relativistic regime:

$$\frac{dv_z}{dt} = v_z \frac{dv_z}{dz}$$

$$\frac{dv_z}{dt} = \frac{q}{m}\left(A\hat{z}e^{i\phi} + c.c.\right)$$

so

$$\frac{d^2\phi}{dz^2} = \frac{\omega}{v_z^3}\frac{q}{m}\left(A\hat{z}e^{i\phi} + c.c.\right)$$

Linearizing: let $\phi = \phi_i + \delta\phi_i$. We introduce space charge parameter k_b as

$$k_b^2 = \sqrt{\frac{\mu}{\epsilon}}\frac{I\psi\tanh(\psi x_h)}{4Vp_zL_y}, \tag{A.57}$$

where

$$\psi = \sqrt{k_z^2 + k_y^2 - \frac{\omega^2}{c^2}}.$$

Writing $\delta\phi_i = \hat{\delta\phi}e^{i\phi_i} + c.c.$, linearized equation of motion is of the form

$$\left(\frac{d^2}{dz^2} + k_b^2\right)\hat{\delta\phi} = \frac{\omega}{v_z^3}\frac{q}{m}A\hat{z}.$$

We define

$$a \equiv \frac{\omega q}{v_z^3 m}A,$$

and examine the power flux:

$$\vec{P} \equiv |P_z|\left(\sigma\hat{z} + \mu\hat{y}\right),$$

where $\sigma = (+)$ for forward wave, $= (-)$ for backward wave, and

$$\mu \equiv \frac{\partial\omega/\partial k_y}{|\partial\omega/\partial k_z|}.$$

W define parameter k_g as

$$k_g \equiv k_{sz}C = \left(\frac{I_b|ez|^3\omega q}{mv_z^3|P_z|}\right)^{1/3},$$

where C is the Pierce parameter, defined as $C = (IZ_p/V)^{1/3}$.

$$\Rightarrow \qquad [(k_z - k_{sz})\sigma + (k_y - k_{sy})\mu]\, a = k_g^3\, \hat{\delta\phi}.$$

Noting that a and $\hat{\delta\phi}$ vary as $e^{i\phi}$, and $\phi \equiv \phi(z,t)$, we have:

$$-\frac{ida}{dz} = (k_z - k_{sz})a.$$

Let $\sigma = -1$ for backward wave and define

$$K \equiv \mu(k_y - k_{sy}) = \frac{\omega}{v_b} - k_{sz} - \frac{i\omega_i}{v_g},$$

we have:

$$\left(\frac{d^2}{dz^2} + k_b^2\right)\hat{\delta\phi} = a, \tag{A.58}$$

$$\frac{ida}{dz} + Ka = k_g^3\, \hat{\delta\phi}. \tag{A.59}$$

On the other hand, if we let $\sigma = 1$ for forward wave, equation (A.59) becomes

$$-\frac{ida}{dz} + Ka = k_g^3\, \hat{\delta\phi}. \tag{A.60}$$

Equations (A.58) and (A.59)(or (A.60)) represent the motion of electrons in beam upon interaction with backward wave (or forward wave) inside the sheath.

A.3.3 Computation Method

For backward waves, the boundary conditions are:

$$\hat{\delta\phi}(0) = 0,$$

$$\frac{\hat{\delta\phi}}{dz}(0) = 0,$$

and

$$a(L_z) = 0.$$

Let a and $\hat{\delta\phi}$ vary as $a = \sum_1^3 a_m e^{-i\phi_m}$ and $\hat{\delta\phi} = \sum_1^3 \hat{\delta\phi}_m e^{-i\phi_m}$.. Noting that $d/dz = ik_m$, combining (A.58) and (A.59) gives us

$$\left(k_b^2 - k_m^2\right)(K - k_m) = k_g^3. \tag{A.61}$$

Or, in dimensionless case:

$$\left(k_b^2 L_z^2 - k_m^2 L_z^2\right)(KL_z - k_m L_z) = k_g^3 L_z^3. \tag{A.62}$$

k_m in equation (A.61) or (A.62) represents the mode of interest and there are three modes since the equation is of third order. The boundary equations stated earlier can now be written as

$$\delta\phi_1 + \delta\phi_2 + \delta\phi_3 = 0,$$

$$k_1 L_z \delta\phi_1 + k_2 L_z \delta\phi_2 + k_3 L_z \delta\phi_3 = 0,$$

and $\left(k_b^2 L_z^2 - k_1^2 L_z^2\right) e^{ik_1 L_z}\delta\phi_1 + \left(k_b^2 L_z^2 - k_2^2 L_z^2\right) e^{ik_2 L_z}\delta\phi_2 + \left(k_b^2 L_z^2 - k_3^2 L_z^2\right) e^{ik_3 L_z}\delta\phi_3 = 0.$

They can be combined to give

$$\begin{aligned}
\delta\phi_1 &= 1, \\
\delta\phi_2 &= \frac{k_1 - k_3}{k_3 - k_2}, \\
\delta\phi_3 &= \frac{k_2 - k_1}{k_3 - k_2},
\end{aligned}$$

leading to

$$\left(k_b^2 L_z^2 - k_1^2 L_z^2\right) e^{ik_1 L_z} + \left(k_b^2 L_z^2 - k_2^2 L_z^2\right) e^{ik_2 L_z} \frac{k_1 - k_3}{k_3 - k_2} + \left(k_b^2 L_z^2 - k_3^2 L_z^2\right) e^{ik_3 L_z} \frac{k_2 - k_1}{k_3 - k_2} = 0. \tag{A.63}$$

Assume all but one parameters in (A.62) are known, we can vary that parameter and solve for the wavenumber k_m's then verify the solutions with (A.63) to find the correct value (for that parameter). Comparing our derivation and values for parameters using the technique described with the numerical analysis in [17], we have the relations between the parameters presented in [17] and ours:

Johnson's parameters	*Parameters used*
CN	$\frac{k_g L_z}{2\pi}$
$(\beta - \beta_e)l$	$k_r L_z$
$Loss$	$20 \log_{10} e^{-k_i L_z}$
QC	$\left(\frac{k_b}{2k_g}\right)^2$

With k_i formulated as

$$k_i = \frac{\omega_i}{\partial\omega/\partial k_z}$$

, we can analyze the Loss Rate as

$$LossRate = 20 \log_{10}(-k_i) = -8.868 k_i \qquad (dB/m).$$

Comparing this result with one given in [17], the unstable starting length can be calculated.

For forward wave, $\sigma = 1$ and using the same notation convention, from (A.58) and (A.60) we have:

$$\left(k_b^2 L_z^2 - k_m^2 L_z^2\right)(K L_z + k_m L_z) = k_g^3 L_z^3, \tag{A.64}$$

which is only different from (A.62) by the after KL_z term. Finding the roots of (A.64) and define the gain as $a(L_z)/a(0)$, we have the equation for total operating mode's total gain:

$$Gain = \frac{\sum(k_b^2 - k_m^2)\delta\phi_m e^{ik_m L_z}}{\sum(k_b^2 - k_m^2)\delta\phi_m}. \tag{A.65}$$

Again, the boundary conditions give the relations between phase amplitudes $\delta\phi_m$

Appendix B: High Frequency Structure Simulator (HFSS) Simulation Techniques

HFSS is a complex and comprehensive software package, capable of simulating various structures under different conditions. This thesis only attempts to give a guide on analyzing the structure of interest and achieve the data required. The first simulation of importance is the one that gives dispersion characteristic of the structure. Then we would want to know about the waves' amplitudes and power flux associated with various modes. These data combined can be sufficient for understanding the physical properties of a slow-wave structure. For a more comprehensive guide, the reader can refer to HFSS's content by choosing *Help* $\rightarrow$ *Content* or pressing *F1*.

B.1 Dispersion Data

For the purpose of analyzing the waves' behavior with different modes, eigenmodes solver is the option that we want to choose here. The step-by-step approach is:

1. Initialize the master-slave boundary. For the simple model, specify the boundary conditions on both longitudinal and transverse directions. This is done through the *HFSS* menu

2. Initialize analysis set up. Different options affect the density and accuracy of the finite element method simulation, and the simulation time. For a good understanding of these options, the reader can refer to the *Help's Content* This is done via *HFSS* $\rightarrow$ *Analysis Setup*

3. Initialize the sweeping-option where the software will sweep through the phase advance specified and fine the resonance frequencies in the range initialized. If the boundary on the side is considered as conducting surface, we only have the master-slave boundary in the $\hat{z}$ and need to sweep the phase in longitudinal direction. In order to test the simple model, we can specify the phase advance in the transverse direction to be 0. This is done via *HFSS* $\rightarrow$ *Opmetric Analysis*

4. After the simulation, we can view and export the result via *HFSS* $\rightarrow$ *Results* $\rightarrow$ *Create Eigenmode Parameters Report*$\rightarrow$ *Rectangular Plot* and choose all the modes.

5. Upon exporting and analyzing the data, the phase advance in degrees can be translated to wave vector in via the relation below. Unit of k_z depends on the unit chosen for the period.

$$k_z = \frac{\pi}{180^o} \frac{phase\ in\ \hat{z}}{period\ in\ \hat{z}}. \tag{B.1}$$

B.2 Fields Data

In order to calculate the Pierce impedance using the data from HFSS, the term is written as

$$Z_p = \frac{\left| \frac{1}{p_z} \int_0^{p_z} \left(E_{z\,real} + iE_{z\,imag} \right) e^{-ik_z z} dz \right|^2}{2k_z^2 \times Power\ Flux}. \tag{B.2}$$

where p_z is the period of the structure in longitudinal direction.

As for the fields, the reader is encouraged to read the *Fields Calculator Cookbook* in the HFSS's *Contents*. See Fig. (B.1). Field calculator can be accessed via *HFSS* $\rightarrow$ *Fields*$\rightarrow$ *Calculator*.

After defining/formulating the field terms that HFSS should extract, the last task is to achieve the desired result with different options. First option of interest should be *Source* because there are many eigenmodes being analyzed. This can be accomplished via *HFSS* $\rightarrow$ *Fields* $\rightarrow$ *Edit source*. The second option is to choose the correct phase advance. This can be done either inside the *Calculator* (as for power flux) or in the *Results*$\rightarrow$ *Create Field Report* $\rightarrow$ *Rectangular Plot* window (as for electric field), depending on what field attribute the user is analyzing.

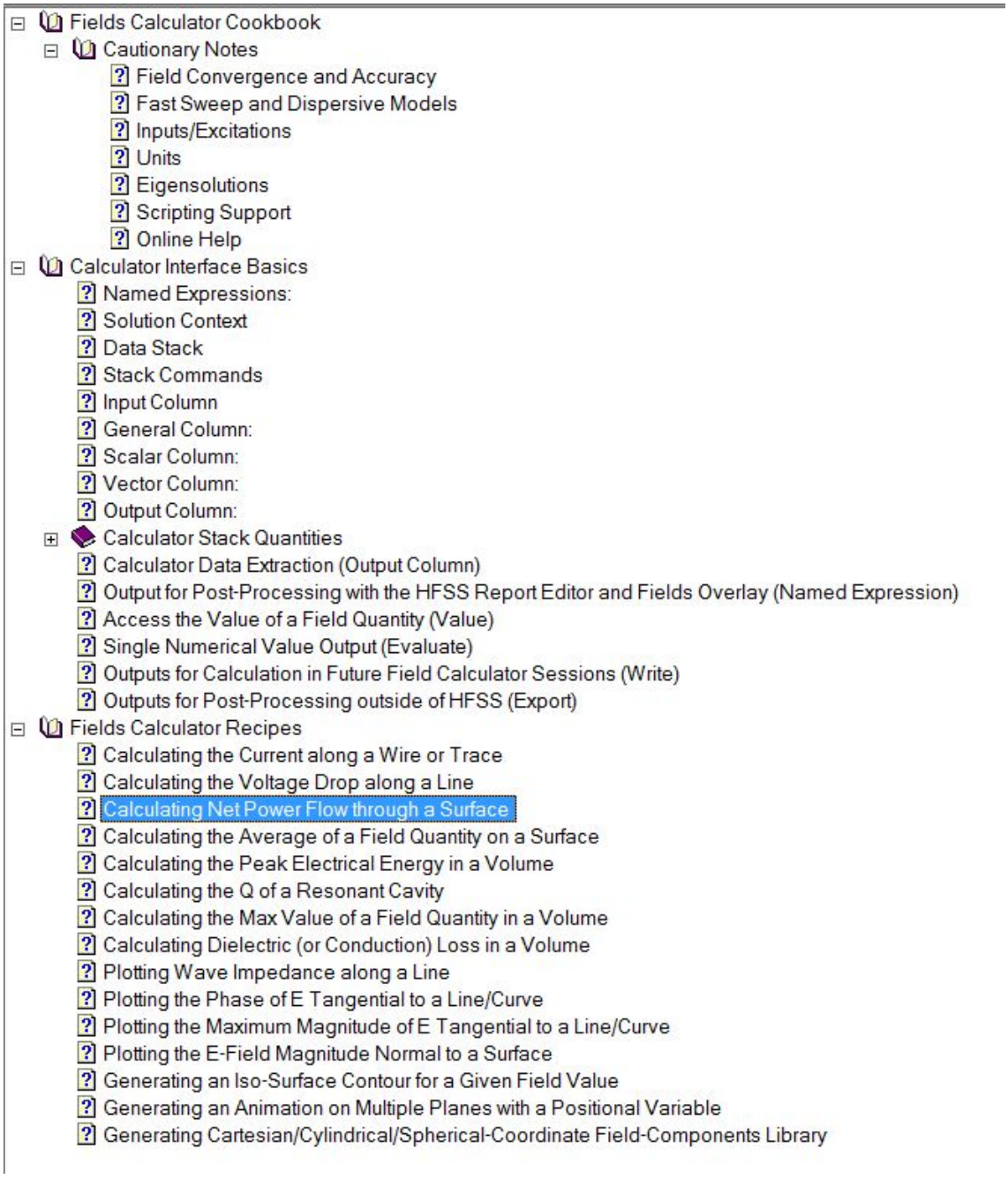

Figure B.1: View of the Field Calculator Cookbook

Bibliography

[1] Encyclopaedia Britannica Online Academic Edition. Electron tubes, April 2014.

[2] R.H. Abrams, B. Levush, A.A. Mondelli, and R.K. Parker. Vacuum electronics for the 21st century. *Microwave Magazine, IEEE*, 2(3):61–72, Sep 2001.

[3] B. Levush, D.K. Abe, J.P. Calame, B.G. Danly, K.T. Nguyen, E.J. Dutkowski, R.H. Abrams, and R.K. Parker. Vacuum electronics: Status and trends. In *Radar Conference, 2007 IEEE*, pages 971–976, April 2007.

[4] C.M. Armstrong. The truth about terahertz. *Spectrum, IEEE*, 49(9):36–41, September 2012.

[5] Brian W.J. McNeil and Neil R. Thompson. X-ray free-electron lasers. *Nature Photonics*, 4(12):814–821, Nov 2010.

[6] John R. Pierce. *Traveling Wave Tubes*. Van Nostrand, New York, USA, 1950.

[7] S.J. Cooke, B. Levush, and T.M. Antonsen. A coupled-cavity slow-wave structure for sheet-beam devices. In *Vacuum Electronics Conference, 2006 held Jointly with 2006 IEEE International Vacuum Electron Sources., IEEE International*, pages 487–488, 2006.

[8] P.B. Larsen, D.K. Abe, S.J. Cooke, B. Levush, T.M. Antonsen, and R.E. Myers. Characterization of a ka-band sheet-beam coupled-cavity slow-wave structure. *Plasma Science, IEEE Transactions on*, 38(6):1244–1254, June 2010.

[9] S. Aditya and R. Arora. Guided waves on a planar helix. *Microwave Theory and Techniques, IEEE Transactions on*, 27(10):860–863, Oct 1979.

[10] A.K. Rashid, S. Aditya, R.K. Arora, and D. Lim. A helical planar slow-wave structure. In *Antennas and Propagation Society International Symposium, 2008. AP-S 2008. IEEE*, pages 1–4, July 2008.

[11] D. Chadha, S. Aditya, and R.K. Arora. Study of planar-helix slow-wave structure for application to travelling-wave tubes. *Microwaves, Optics and Antennas, IEE Proceedings H*, 131(1):14–20, February 1984.

[12] Chengfang Fu, Yanyu Wei, Wenxiang Wang, and Yubin Gong. Dispersion characteristics of a rectangular helix slow-wave structure. *Electron Devices, IEEE Transactions on*, 55(12):3582–3589, Dec 2008.

[13] Guo Guo, Yanyu Wei, Minghao Zhang, G. Travish, Lingna Yue, Jin Xu, Hairong Yin, Minzhi Huang, Yubin Gong, and Wenxiang Wang. Novel folded frame slow-wave structure for millimeter-wave traveling-wave tube. *Electron Devices, IEEE Transactions on*, 60(11):3895–3900, Nov 2013.

[14] P.B. Larsen, D.K. Abe, S.J. Cooke, B. Levush, and Y.N. Pchelnikov. Characterization of a ka-band sheet-beam coupled-cavity slow-wave structure: Simulation and experiment. In *Plasma Science - Abstracts, 2009. ICOPS 2009. IEEE International Conference on*, pages 1–1, June 2009.

[15] L.B. Nguyen, T.M. Antonsen, and G.S. Nusinovich. Open planar sheath slow-wave structure. In *Vacuum Electronics Conference (IVEC), 2013 IEEE 14th International*, pages 1–2, May 2013.

[16] L.B. Nguyen, T.M. Antonsen, and G.S. Nusinovich. Open planar sheath slow-wave structure. In *Plasma Science (ICOPS), 2013 Abstracts IEEE International Conference on*, pages 1–1, June 2013.

[17] H. R. Johnson. Backward-wave oscillators. *Proceedings of the IRE*, pages 684–697, 1955.

[18] T.M. Antonsen, P. Safier, D.P. Chernin, and B. Levush. Stability of traveling-wave amplifiers with reflections. *Plasma Science, IEEE Transactions on*, 30(3):1089–1107, Jun 2002.

[19] David K. Cheng. *Field and Wave Electromagnetics*. Addison-Wesley, New York, USA, 1992.

[20] John D. Jackson. *Classical Electrodynamics*. Wiley, Hoboken, NJ, USA, 1999.